

MIT Open Access Articles

*Upwinding and artificial viscosity for robust discontinuous
Galerkin schemes of two-phase flow in mass conservation form*

The MIT Faculty has made this article openly available. **Please share**
how this access benefits you. Your story matters.

As Published: <https://doi.org/10.1007/s10596-020-09999-6>

Publisher: Springer International Publishing

Persistent URL: <https://hdl.handle.net/1721.1/131988>

Version: Author's final manuscript: final author's manuscript post peer review, without publisher's formatting or copy editing

Terms of use: Creative Commons Attribution-Noncommercial-Share Alike



Upwinding and artificial viscosity for robust discontinuous Galerkin schemes of two-phase flow in mass conservation form

Cite this article as: Savithru Jayasinghe, David L. Darmofal, Steven R. Allmaras, Eric Dow and Marshall C. Galbraith, Upwinding and artificial viscosity for robust discontinuous Galerkin schemes of two-phase flow in mass conservation form, *Computational Geosciences* doi: [10.1007/s10596-020-09999-6](https://doi.org/10.1007/s10596-020-09999-6)

This Author Accepted Manuscript is a PDF file of a an unedited peer-reviewed manuscript that has been accepted for publication but has not been copyedited or corrected. The official version of record that is published in the journal is kept up to date and so may therefore differ from this version.

Terms of use and reuse: academic research for non-commercial purposes, see here for full terms. <http://www.springer.com/gb/open-access/authors-rights/aam-terms-v1>

Upwinding and artificial viscosity for robust discontinuous Galerkin schemes of two-phase flow in mass conservation form

Savithru Jayasinghe · David L. Darmofal · Steven R. Allmaras ·
Eric Dow · Marshall C. Galbraith

Received: date / Accepted: date

Abstract High-order discretizations have become increasingly popular across a wide range of applications, including reservoir simulation. However, the lack of stability and robustness of these discretizations for advection-dominant problems prevent them from being widely adopted. This paper presents work towards improving the stability and robustness of the discontinuous Galerkin (DG) finite element scheme, for advection-dominant two-phase flow problems in particular. A linearized analysis of the two-phase flow equations is used to show that a standard DG discretization of the two-phase flow equations in mass conservation form results in a neutrally stable semi-discrete system in the advection-dominant limit. Further, the analysis is also used to propose additional terms to the DG method which linearly stabilize the discretization. These additional terms are derived by comparing the linearized equations in mass conservation form against an upwinded pressure-saturation form of the equations. Next, a partial differential equation-based artificial viscosity method is proposed for the Buckley-Leverett and two-phase flow equations, as a means of mitigating Gibbs oscillations in high-order discretizations and ensuring convergence to physical solutions. The modified DG method with artificial viscosity

is demonstrated on a two-phase flow problem with heterogeneous rock permeabilities, where the high-order discretizations significantly outperform a conventional first-order approach in terms of computational cost required to achieve a given level of error in an output of interest.

Keywords two-phase flow · discontinuous Galerkin · linear stability · upwinding · artificial viscosity · high-order

1 Introduction

Over the last few decades, porous media flow simulations have primarily been computed using *low-order* discretizations such as the finite volume (FV) [4, 21] and finite difference methods [42]. Although the term “low-order” typically refers to numerical methods that have at most second-order accuracy in space and time [52], most reservoir simulation tools used in practice are first-order accurate in both space and time for transport quantities (e.g. single-point upstream-weighted FV, backward Euler time-marching). Conventional methods such as the widely used two-point flux approximation (TPFA) finite volume method are in fact only consistent on K-orthogonal grids [18], where the grid cells are aligned with the principal directions of the permeability tensor. Multi-point flux approximation (MPFA) methods and its derivatives overcome this limitation by producing consistent discretizations even on problems with complex unstructured grids and full tensor permeabilities, but at the expense of extended stencils and a loss of monotonicity and a discrete maximum principle [1, 53, 2, 54].

In recent years, there has been a growing interest towards using high-order methods to solve porous

This research was supported through a Research Agreement with Saudi Aramco, a Founding Member of the MIT Energy Initiative (<http://mitei.mit.edu/>), with technical monitors Dr. Ali Dogru and Dr. Eric Dow.

S. Jayasinghe · D. Darmofal · S. Allmaras · M. Galbraith
Massachusetts Institute of Technology, 77 Massachusetts
Ave., Cambridge, MA
E-mail: savithru@mit.edu, darmofal@mit.edu,
galbraim@mit.edu, allmaras@mit.edu

E. Dow
Aramco Americas, 400 Technology Square, Cambridge, MA
E-mail: eric.dow@aramcoamericas.com

media flow problems. Finite element methods, such as the discontinuous Galerkin (DG) method considered in this work, offer a means to obtain high-order accurate solutions by increasing the order of the polynomial basis functions used to represent the solution, and have been successfully applied to single-phase [48, 47, 36], two-phase [46, 47, 19, 34, 20, 3, 10, 29], and three-phase [37, 45] flow problems. Additional properties such as local mass conservation on the primal mesh and ease of implementation on unstructured grids make the DG method a competitive alternative to the conventional low-order methods. However, high-order discretizations are known to suffer from stability and robustness issues, especially on problems with discontinuous or nearly-discontinuous solutions. Two-phase flows, and multiphase flows in general, give rise to sharp or discontinuous solution features such as saturation fronts, especially in the regime of low capillarity. In conventional methods such as the finite volume method with TPFA, the discretization is stabilized by fully upwinding saturation-dependent quantities, such as the relative permeabilities, based on the local flow direction obtained through the potential gradient [42]. Alternate approaches to flux upwinding have also been demonstrated for FV discretizations [32], with the aim of reducing nonlinear convergence issues caused by the non-differentiability of the conventional upwinding operator.

The objective of this work is to investigate the stability of high-order discretizations for advection-dominant two-phase flow problems. In particular, this work aims to improve the stability and robustness of the DG finite element method for this class of problems. High-order linear discretizations produce Gibbs oscillations in regions around discontinuities in the solution (e.g. saturation fronts) and under-resolved features more generally. These unphysical oscillations may propagate and pollute the solution downstream. In the context of multiphase flow problems where saturation is a primary solution variable, such oscillations may give rise to unphysical values of saturation and cause the numerical solution to converge to entropy-violating solutions [4, 27]. Shock-capturing methods aim to mitigate or eliminate unphysical oscillations by modifying the discretization through some form of nonlinearity. A wide body of literature of such methods exists, but only a few of the most relevant ones are reviewed below.

1.1 Slope limiters

The goal of using slope limiters (or flux limiters) is to limit solution gradients to physical values, in order to avoid spurious oscillations that may occur in high-order numerical solutions near solution discontinuities. The

use of slope limiters make the numerical solutions total variation diminishing (TVD), which implies that no new local extrema are created, the values of local minima do not decrease, and the values of local maxima do not increase. One of the first applications of slope limiters to DG schemes was in a series of papers by Cockburn and Shu, where a Runge-Kutta discontinuous Galerkin method (RKDG) was used with minmod-type slope limiters [14, 13, 12, 16]. In the context of reservoir simulation, slope limiters have been used with DG methods to discretize the saturation equation in two-phase flow problems [11, 39, 26], and the species mass balance equations in compositional flow problems [25, 37]. However, one of the major disadvantages of slope limiting methods is that they do not work well with implicit time-marching schemes, since the clamping of higher-order solution modes near discontinuities and the non-differentiability of most limiters tend to produce ill-conditioned Jacobian matrices, resulting in poor convergence behaviors [51].

1.2 Artificial viscosity

An alternate method is to explicitly add extra dissipation into the problem by introducing diffusion terms to the governing partial differential equation (PDE). A simple approach is to increase the amount of physical dissipation in the problem, for example by increasing capillary effects [27], but this has the downside of degrading the accuracy of the solution globally. Hence, a better approach would be to add artificial viscosity in a controlled manner such that the artificial viscosity is zero in smooth regions of the solution and non-zero only in the vicinity of shocks where oscillations occur. Furthermore, the artificial viscosity must vanish as $h \rightarrow 0$, in order to ensure the consistency of the numerical discretization.

The amount of artificial viscosity added may be driven by the residuals of the original PDEs or some other predefined *sensor* quantity that is a function of the local solution. The work of Johnson et al [33], Bassi and Rebay [7], and Hartmann and Houston [24], successfully demonstrate the use of residual-based artificial viscosity to control oscillations in finite element solutions of the compressible Euler equations. Similar residual-based methods have been applied to miscible displacement and three-phase flow problems in [50, 49]. The entropy viscosity method introduced in [22] stabilizes the solution by adding an artificial viscosity that is proportional to the entropy residual, and is demonstrated for nonlinear scalar conservation laws and the Euler equations using a continuous Galerkin (CG) method.

Jiang and Tchepeli [31] present an artificial dissipation-based continuation method for multiphase flow problems, where the level of dissipation is controlled by a continuation parameter and the local wave speed. The application of their method to a 2D heterogeneous two-phase problem results in a significantly better nonlinear convergence behavior compared to a standard Newton method used in reservoir simulation.

The amount of artificial viscosity added can also be controlled by a sensor variable that detects discontinuities and under-resolved regions in the solution. In [44], Persson and Peraire propose an artificial viscosity driven by a discontinuity sensor, which uses the decay rate of higher order solution modes to identify regions with large jumps in the solution. Their method is demonstrated for the 1D Burgers' equation and 2D Euler equations using the DG method. In [38], Moro et al use a dilation-based sensor to compute the artificial viscosity for Navier-Stokes problems, which exploits the presence of strong negative velocity divergences (dilation) near shocks. Barter and Darmofal [5] show that a piecewise-constant artificial viscosity field can introduce spurious oscillations on the gradient of the solution which may corrupt the downstream solution. Hence, they propose a PDE-based artificial viscosity method, where an additional equation is solved in a coupled manner with the original PDE(s) in order to determine the distribution of artificial viscosity over the domain. A reaction-diffusion PDE is used for the auxiliary equation which smoothly diffuses away the artificial viscosity generated by the reaction term. The application of this approach to compressible Navier-Stokes problems demonstrates greater solution accuracy and smoother artificial viscosity distributions compared to piecewise-constant approaches. Unlike slope limiting techniques, artificial viscosity methods obtained by modifying the governing PDE(s) can be discretized using implicit schemes in a straight-forward manner.

1.3 Outline of paper

Section 2 presents the mass conservation form of the two-phase flows equations considered in this work. Section 3 reviews the discontinuous Galerkin method for a general unsteady conservation law with advection fluxes, diffusive fluxes and solution-dependent source terms. Section 4 presents a linearized stability analysis of the DG method for the two-phase flow equations, and derives additional stabilization terms for upwinding the underlying saturation equation. Further, numerical results on a 1D test problem are presented to show the effect of the stabilization terms on the linear stability of the discretization. Section 5 presents a PDE-based

artificial viscosity method applicable to high-order discretizations of the Buckley-Leverett and two-phase flow equations. Section 6 demonstrates the high-order DG method with artificial viscosity on a two-phase flow problem with heterogeneous rock permeabilities, and compares its results with those from a conventional finite volume method.

2 Governing equations for two-phase flow

In this work, the governing partial differential equations for two-phase flow are assumed to be in the mass conservation form for each of the two phases in the porous medium, where the non-wetting phase pressure (p_n) and the wetting phase saturation (S_w) are chosen to be the primary solution variables. The coupled, nonlinear system of equations for the conservation of mass of the wetting (w) and non-wetting (n) phases is given below,

$$\frac{\partial}{\partial t} (\rho_w \phi S_w) - \nabla \cdot (\rho_w \lambda_w \mathbf{K} \nabla p_w) = \rho_w q_w \quad (1)$$

$$\frac{\partial}{\partial t} (\rho_n \phi (1 - S_w)) - \nabla \cdot (\rho_n \lambda_n \mathbf{K} \nabla p_n) = \rho_n q_n, \quad (2)$$

$$\forall \vec{x} \in \Omega_s, t \in I,$$

where ρ_w and ρ_n are the phase densities, ϕ is the rock porosity, \mathbf{K} is the rock permeability tensor, p_w is the wetting-phase pressure, and q_w and q_n are source terms. The relative phase mobilities are defined as,

$$\lambda_w = \frac{k_{rw}}{\mu_w} \quad \text{and} \quad \lambda_n = \frac{k_{rn}}{\mu_n}, \quad (3)$$

where k_{rw} and k_{rn} are the relative permeability functions, and μ_w and μ_n are the fluid viscosities of the wetting and non-wetting phases respectively. The pressure and saturation variables also satisfy the following closure relations,

$$p_w + p_c = p_n, \quad (4)$$

$$S_w + S_n = 1, \quad (5)$$

where $p_c(S_w)$ is the capillary pressure. The spatial domain is denoted by $\Omega_s \subset \mathbb{R}^d$, and $I = [0, T]$ is the time interval of interest.

3 Discontinuous Galerkin discretization

This section describes the discontinuous Galerkin finite element discretization for a general unsteady conservation law of the form,

$$\begin{aligned} \frac{\partial}{\partial t} (\mathbf{F}^{\text{temp}}(\mathbf{u})) + \nabla \cdot (\vec{\mathbf{F}}^{\text{adv}}(\mathbf{u}) - \vec{\mathbf{F}}^{\text{diff}}(\mathbf{u}, \nabla \mathbf{u})) \\ + \mathbf{S}(\mathbf{u}, \nabla \mathbf{u}, \vec{x}, t) = \mathbf{0}, \quad \forall \vec{x} \in \Omega_s, t \in I \end{aligned} \quad (6)$$

where $\mathbf{u} \in \mathbb{R}^m$ is the m -variable state vector, and \vec{x} represents the spatial coordinates in the d -dimensional domain Ω_s . $\mathbf{F}^{\text{temp}}(\mathbf{u}) \in \mathbb{R}^m$ represents the temporal or unsteady flux, whereas $\vec{\mathbf{F}}^{\text{adv}}(\mathbf{u}) \in \mathbb{R}^{m \times d}$ and $\vec{\mathbf{F}}^{\text{diff}}(\mathbf{u}, \nabla \mathbf{u}) \in \mathbb{R}^{m \times d}$ represent the spatial advective and diffusive fluxes respectively. Any solution-, coordinate- and time-dependent source terms are given by $\mathbf{S}(\mathbf{u}, \nabla \mathbf{u}, \vec{x}, t) \in \mathbb{R}^m$. The diffusive flux is also assumed to be a linear function of $\nabla \mathbf{u}$, written as,

$$\vec{\mathbf{F}}^{\text{diff}}(\mathbf{u}, \hat{\nabla} \mathbf{u}) = \vec{\mathbf{A}}(\mathbf{u}) \nabla \mathbf{u}, \quad (7)$$

where $\vec{\mathbf{A}}(\mathbf{u})$ is the diffusion tensor. The boundary conditions of the problem are imposed using an operator \mathcal{B} defined as,

$$\mathcal{B}(\mathbf{u}, \vec{\mathbf{F}}^{\text{adv}}(\mathbf{u}) \cdot \vec{n}, \vec{\mathbf{F}}^{\text{diff}}(\mathbf{u}, \hat{\nabla} \mathbf{u}) \cdot \vec{n}, \vec{x}; BC) = 0, \quad \forall \vec{x} \in \partial \Omega_s, \quad (8)$$

where \vec{n} is the unit normal vector on the boundary $\partial \Omega_s$ and BC represents the boundary condition data.

The unsteady conservation law described above can be solved with a time-marching DG method, or a space-time DG method where the d -dimensional unsteady problem is treated as a $(d+1)$ -dimensional steady problem [27, 29]. However, this paper only considers time-marching DG methods.

The DG discretization seeks a solution in a finite dimensional function space $V_{h,p}$, which is defined as,

$$V_{h,p} \equiv \{ \mathbf{v} \in [L^2(\Omega_s)]^m : \mathbf{v}|_\kappa \in [\mathcal{P}^p(\kappa)]^m, \forall \kappa \in \mathcal{T}_h \}. \quad (9)$$

$V_{h,p}$ represents the piecewise discontinuous solution space of p^{th} -order polynomials on each element of \mathcal{T}_h , where \mathcal{T}_h is a triangulation of the domain Ω_s into non-overlapping elements κ of characteristic size h .

Multiplying Eq. 6 by a test function $\mathbf{v}_{h,p} \in V_{h,p}$ and integrating by parts yields the weak formulation of the governing equation. Solving this weak formulation involves finding a solution $\mathbf{u}_{h,p} \in V_{h,p}$ that satisfies,

$$\begin{aligned} \mathcal{R}_{h,p}(\mathbf{u}_{h,p}, \mathbf{v}_{h,p}) &= \sum_{\kappa \in \mathcal{T}_h} \int_{\kappa} \mathbf{v}_{h,p}^T \frac{\partial}{\partial t} (\mathbf{F}^{\text{temp}}(\mathbf{u}_{h,p})) d\Omega_s + \mathcal{R}_{h,p}^s(\mathbf{u}_{h,p}, \mathbf{v}_{h,p}) \\ &= 0, \quad \forall \mathbf{v}_{h,p} \in V_{h,p}. \end{aligned} \quad (10)$$

The semi-linear form associated with the spatial residual, $\mathcal{R}_{h,p}^s : V_{h,p} \times V_{h,p} \rightarrow \mathbb{R}$, is composed of three terms,

$$\mathcal{R}_{h,p}^s(\mathbf{u}, \mathbf{v}) = \mathcal{R}_{h,p}^{\text{adv}}(\mathbf{u}, \mathbf{v}) + \mathcal{R}_{h,p}^{\text{diff}}(\mathbf{u}, \mathbf{v}) + \mathcal{R}_{h,p}^{\text{source}}(\mathbf{u}, \mathbf{v}), \quad (11)$$

where $\mathcal{R}_{h,p}^{\text{adv}}(\mathbf{u}, \mathbf{v})$, $\mathcal{R}_{h,p}^{\text{diff}}(\mathbf{u}, \mathbf{v})$ and $\mathcal{R}_{h,p}^{\text{source}}(\mathbf{u}, \mathbf{v})$ represent the contributions of the advective, diffusive and source terms to the weighted residual, respectively.

3.1 Advective flux discretization

The DG discretization of the advective flux term is given by,

$$\begin{aligned} \mathcal{R}_{h,p}^{\text{adv}}(\mathbf{u}, \mathbf{v}) &= - \sum_{\kappa \in \mathcal{T}_h} \int_{\kappa} \nabla \mathbf{v}^T \cdot \vec{\mathbf{F}}^{\text{adv}}(\mathbf{u}) d\Omega_s \\ &\quad + \sum_{f \in \Gamma_I} \int_f (\mathbf{v}^+ - \mathbf{v}^-)^T \mathcal{H}(\mathbf{u}^+, \mathbf{u}^-; \vec{n}^+) d\Gamma \\ &\quad + \sum_{f \in \Gamma_B} \int_f \mathbf{v}^{+T} \mathcal{H}^B(\mathbf{u}^+, \mathbf{u}^B(\mathbf{u}^+; BC); \vec{n}^+) d\Gamma, \end{aligned} \quad (12)$$

where $(\cdot)^+$ and $(\cdot)^-$ denote the trace values evaluated from opposite sides of a face f and \vec{n}^+ is the unit normal vector pointing from the $(+)$ side to the $(-)$ side of a face. Γ_I and Γ_B represent the set of interior and boundary faces, respectively. \mathcal{H} and \mathcal{H}^B are numerical flux functions which produce unique, upwinded fluxes on the interior and boundary faces, respectively. At the domain boundaries, the numerical flux \mathcal{H}^B is evaluated using a boundary state \mathbf{u}^B , which itself is a function of both the interior state \mathbf{u}^+ and the user-specified boundary condition data BC .

3.2 Diffusive flux discretization

In this work, the diffusive flux terms are discretized using the second method proposed by Bassi and Rebay (BR2) [8, 9]. For notational simplicity, the jump $[\![\cdot]\!]$ and average $\{\cdot\}$ operators are defined for a scalar s and a vector \vec{v} on an interior face as,

$$\begin{aligned} \{s\} &= \frac{1}{2}(s^+ + s^-), & \{\vec{v}\} &= \frac{1}{2}(\vec{v}^+ + \vec{v}^-) \\ [\![s]\!] &= s^+ \vec{n}^+ + s^- \vec{n}^-, & [\![\vec{v}]\!] &= \vec{v}^+ \cdot \vec{n}^+ + \vec{v}^- \cdot \vec{n}^-, \end{aligned} \quad (13)$$

where $\vec{n}^- = -\vec{n}^+$.

The semi-linear form for the diffusive fluxes can then be written as follows,

$$\begin{aligned} \mathcal{R}_{h,p}^{\text{diff}}(\mathbf{u}, \mathbf{v}) = & \sum_{\kappa \in \mathcal{T}_h} \int_{\kappa} \nabla \mathbf{v}^T \cdot (\tilde{\mathbf{A}}(\mathbf{u}) \nabla \mathbf{u}) \, d\Omega_s \\ & - \sum_{f \in \Gamma_I} \int_f \llbracket \mathbf{v} \rrbracket^T \cdot \left\{ \tilde{\mathbf{A}}(\mathbf{u}) \nabla \mathbf{u} \right\} \, d\Gamma \\ & - \sum_{f \in \Gamma_I} \int_f \llbracket \mathbf{v} \rrbracket^T \cdot \left\{ \tilde{\mathbf{A}}(\mathbf{u}) \eta_f \tilde{\mathbf{r}}_f(\llbracket \mathbf{u} \rrbracket) \right\} \, d\Gamma \\ & - \sum_{f \in \Gamma_I} \int_f \left\{ \tilde{\mathbf{A}}^T(\mathbf{u}) \nabla \mathbf{v} \right\}^T \cdot \llbracket \mathbf{u} \rrbracket \, d\Gamma \\ & - \sum_{f \in \Gamma_B} \int_f (\mathbf{v}^+ \tilde{\mathbf{n}}^+)^T \cdot \tilde{\mathbf{A}}_B \nabla \mathbf{u}^B \, d\Gamma \\ & - \sum_{f \in \Gamma_B} \int_f (\mathbf{v}^+ \tilde{\mathbf{n}}^+)^T \cdot \tilde{\mathbf{A}}_B \eta_f \tilde{\mathbf{r}}_f((\mathbf{u}^+ - \mathbf{u}^B) \tilde{\mathbf{n}}^+) \, d\Gamma, \\ & - \sum_{f \in \Gamma_B} \int_f \left(\tilde{\mathbf{A}}_B^T \nabla \mathbf{v}^+ \right)^T \cdot (\mathbf{u}^+ - \mathbf{u}^B) \cdot \tilde{\mathbf{n}}^+ \, d\Gamma \end{aligned} \quad (14)$$

where the boundary fluxes are set using $\mathbf{u}^B(\mathbf{u}^+; BC)$, $\tilde{\mathbf{A}}_B(\mathbf{u}^B)$, and $\nabla \mathbf{u}^B(\nabla \mathbf{u}^+; BC)$. The lifting operator $\tilde{\mathbf{r}}_f : [V_{h,p}(f)]^d \rightarrow [V_{h,p}]^d$, essentially penalizes jumps in the solution across a face, and is defined as follows for an interior face f ,

$$\sum_{\kappa \in \kappa_f} \int_{\kappa} \tilde{\mathbf{s}}^T \cdot \tilde{\mathbf{r}}_f(\tilde{\mathbf{g}}) \, d\Omega = - \int_f \{\tilde{\mathbf{s}}\}^T \cdot \tilde{\mathbf{g}} \, d\Gamma, \quad (15)$$

$$\forall \tilde{\mathbf{s}}, \tilde{\mathbf{g}} \in [V_{h,p}]^d$$

where κ_f is the set of elements sharing the face f . For a boundary face f , the lifting operator is defined as,

$$\int_{\kappa_B} \tilde{\mathbf{s}}^T \cdot \tilde{\mathbf{r}}_f(\tilde{\mathbf{g}}) \, d\Omega = - \int_f \tilde{\mathbf{s}}^+{}^T \cdot \tilde{\mathbf{g}} \, d\Gamma, \quad (16)$$

$$\forall \tilde{\mathbf{s}}, \tilde{\mathbf{g}} \in [V_{h,p}]^d$$

where κ_B is the element containing the boundary face. The stability of the DG discretization requires that the BR2 stabilization parameter, η_f , is greater than or equal to the number of faces in an element [23]. In this work, η_f is set to twice the number of faces in an element.

3.3 Source discretization

The discretization of the source terms follows the formulation proposed by Bassi *et al.* in [6] where the state

gradients are augmented with a global lifting operator as shown below.

$$\mathcal{R}_{h,p}^{\text{source}}(\mathbf{u}; \mathbf{v}) = \sum_{\kappa \in \mathcal{T}_h} \int_{\kappa} \mathbf{v}^T \mathbf{S}(\mathbf{u}, \nabla \mathbf{u} + \tilde{\mathbf{r}}_{\text{glob}}(\mathbf{u}), \tilde{\mathbf{x}}) \, d\Omega, \quad (17)$$

where the global lifting operator $\tilde{\mathbf{r}}_{\text{glob}} : \mathcal{V}_{h,p} \rightarrow [\mathcal{V}_{h,p}]^{d+1}$ is defined as the sum of local lifting operators,

$$\tilde{\mathbf{r}}_{\text{glob}}(\mathbf{u}) = \sum_{f \in \Gamma_I} \tilde{\mathbf{r}}_f(\llbracket \mathbf{u} \rrbracket) + \sum_{f \in \Gamma_B} \tilde{\mathbf{r}}_f((\mathbf{u}^+ - \mathbf{u}^B) \tilde{\mathbf{n}}^+). \quad (18)$$

This approach was also shown to be asymptotically dual-consistent by Oliver in [41]. Dual-consistent or asymptotically dual-consistent discretizations have been observed to yield higher convergence rates for an output of interest, compared to dual-inconsistent schemes [40].

3.4 Solution method

Expressing the solution $\mathbf{u}_{h,p}$ and the test function $\mathbf{v}_{h,p}$ in Eq. 10 in terms of element-wise discontinuous polynomial basis functions yields a set of differential equations which is discretized in time using an implicit time-marching scheme such as the backward Euler method. The resulting nonlinear system of equations at each time-step is solved using Newton's method with a line-search algorithm. The ensuing linear systems for 1D problems in this work are solved using the UMFPACK [17] sparse direct solver, while 2D problems are solved using a restarted generalized minimal residual (GMRES) method with an ILU(k) preconditioner.

4 Upwinding via linearized analysis

It is well known that the incompressible two-phase flow equations possess a hyperbolic-elliptic nature due to the presence of an underlying elliptic pressure equation and a hyperbolic (or near-hyperbolic) saturation transport equation. Under assumptions of zero capillary pressure and one dimensional flow, this saturation equation reduces to the well-known Buckley-Leverett equation. However, if the two-phase flow equations are expressed in mass conservation form, as is done in most industrial practices, the equations "appear" as a pair of coupled parabolic equations, effectively concealing their hyperbolic nature. Therefore, if the spatial fluxes inside the divergence operators in Eqs. 1 - 2 are interpreted as diffusive fluxes and discretized using a standard DG method such as the BR2 method given in Eq. 14, it

results in a centered discretization of the spatial operators. However, a centered discretization of an advection-dominant problem is known to cause oscillations and instabilities. This therefore suggests that the DG discretization of the spatial operators in Eqs. 1 - 2 requires some modification, typically an upwinding bias, in order to be stable in the advection-dominant limit.

This section presents the derivation of such a modification to the BR2 scheme, obtained via a linearized analysis of the two-phase flow equations in both continuous and discrete settings. The various steps of the analysis are summarized in Figure 1, where the blue blocks represent the continuous equations, yellow blocks represent the standard DG weak form equations that result in centered discretizations, and the green blocks represent modified DG weak form equations where the saturation behavior has been correctly upwinded. The analysis first linearizes the continuous two-phase flow equations in mass conservation form and then manipulates them into a linearized pressure-saturation form (bottom-left block). This is then discretized using the DG method to obtain a centered discretization for the linearized pressure equation, and an appropriately upwinded discretization for the linearized saturation equation (bottom-right block). The desired modification terms to the DG weak form (dashed arrow) are designed such that a similar linearization of the final modified DG discretization (top-right block) would produce the same discrete linearized pressure-saturation form.

Although the analysis is performed using the BR2 scheme, it is expected that the resulting modifications to the discretization will be equally applicable to other centered DG diffusive flux discretizations such as the local discontinuous Galerkin method (LDG) [15], compact discontinuous Galerkin method (CDG) [43] and the interior penalty Galerkin methods (SIPG, IIPG).

4.1 Continuous linearized analysis

Consider a solution that is expressed as a perturbation about some base pressure distribution $\bar{p}_n(\vec{x}, t)$ and a constant saturation value \bar{S}_w ,

$$p_n(\vec{x}, t) = \bar{p}_n(\vec{x}, t) + p'_n(\vec{x}, t), \quad (19)$$

$$S_w(\vec{x}, t) = \bar{S}_w + S'_w(\vec{x}, t), \quad (20)$$

where the base solutions \bar{p}_n and \bar{S}_w satisfy Eqs. 1 - 2. Substituting the above perturbed solutions into Eqs. 1 - 2, canceling out the base flow terms, and ignoring products of perturbations yields the linearized incom-

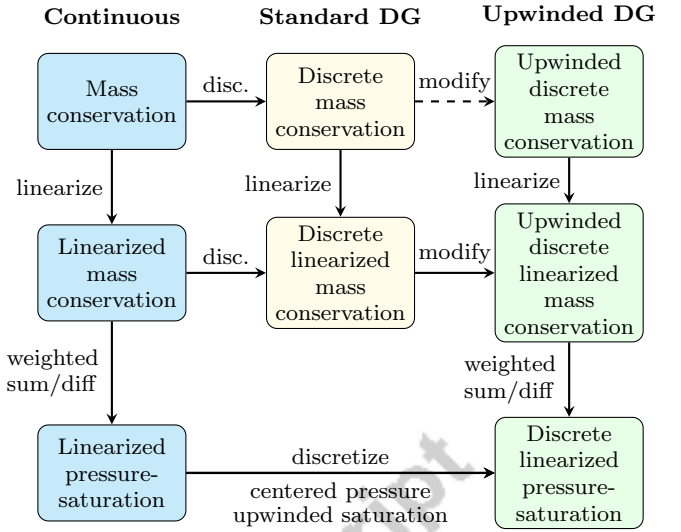


Fig. 1 Outline of linearized analysis for deriving upwinding modifications.

pressible two-phase flow equations,

$$\begin{aligned} \rho_w \phi \frac{\partial S'_w}{\partial t} + \nabla \cdot (-\rho_w \bar{\lambda}_{ws} \mathbf{K} \nabla \bar{p}_w S'_w) \\ - \nabla \cdot (\rho_w \bar{\lambda}_w \mathbf{K} \nabla p'_w) = 0, \end{aligned} \quad (21)$$

$$\begin{aligned} -\rho_n \phi \frac{\partial S'_w}{\partial t} + \nabla \cdot (-\rho_n \bar{\lambda}_{ns} \mathbf{K} \nabla \bar{p}_n S'_w) \\ - \nabla \cdot (\rho_n \bar{\lambda}_n \mathbf{K} \nabla p'_n) = 0, \end{aligned} \quad (22)$$

where $\bar{\lambda}_{\alpha s} = \frac{d\lambda_\alpha}{dS_w} \big|_{\bar{S}_w}$, $\bar{p}_w = \bar{p}_n - p_c(\bar{S}_w)$, $p'_w = p'_n - \bar{p}_{cs} S'_w$, and $\bar{p}_{cs} = \frac{dp_c}{dS_w} \big|_{\bar{S}_w}$.

Taking the weighted difference of the linearized equations, $\rho_n \bar{\lambda}_n \times (\text{Eq. 21}) - \rho_w \bar{\lambda}_w \times (\text{Eq. 22})$, yields a parabolic “saturation” equation,

$$\begin{aligned} \rho_w \rho_n (\bar{\lambda}_w + \bar{\lambda}_n) \phi \frac{\partial S'_w}{\partial t} \\ + \nabla \cdot (\rho_w \rho_n (-\bar{\lambda}_{ws} \bar{\lambda}_n \mathbf{K} \nabla \bar{p}_w + \bar{\lambda}_w \bar{\lambda}_{ns} \mathbf{K} \nabla \bar{p}_n) S'_w) \\ - \nabla \cdot (\rho_w \rho_n \bar{\lambda}_w \bar{\lambda}_n \mathbf{K} (\nabla p'_w - \nabla p'_n)) = 0. \end{aligned} \quad (23)$$

Dividing through by $\rho_w \rho_n (\bar{\lambda}_w + \bar{\lambda}_n) \phi$, and noting that $\nabla p'_w - \nabla p'_n = -\nabla p'_c = -\bar{p}_{cs} \nabla S'_w$ allows the saturation equation above to be written in the form of an unsteady advection-diffusion PDE,

$$\frac{\partial S'_w}{\partial t} + \nabla \cdot (\vec{V} S'_w - \bar{\mathbf{D}} \nabla S'_w) = 0, \quad (24)$$

where the advection velocity \vec{V} and the diffusion coefficient $\bar{\mathbf{D}}$ are given by,

$$\vec{V} = \frac{-\bar{\lambda}_w \bar{\lambda}_n \mathbf{K} \nabla \bar{p}_w + \bar{\lambda}_w \bar{\lambda}_n \mathbf{K} \nabla \bar{p}_n}{\phi(\bar{\lambda}_w + \bar{\lambda}_n)} \quad (25)$$

$$\bar{\mathbf{D}} = \frac{-\bar{\lambda}_w \bar{\lambda}_n \bar{p}_{cs} \mathbf{K}}{\phi(\bar{\lambda}_w + \bar{\lambda}_n)}. \quad (26)$$

Note that the saturation equation reduces to a purely hyperbolic PDE when there are no capillary effects ($p_c = 0$).

Similarly, taking the weighted sum of the linearized equations, $\rho_n \times (\text{Eq. 21}) + \rho_w \times (\text{Eq. 22})$, yields an elliptic “pressure” equation,

$$\begin{aligned} \nabla \cdot (\rho_w \rho_n (\bar{\lambda}_w \mathbf{K} \nabla p'_w + \bar{\lambda}_n \mathbf{K} \nabla p'_n)) \\ = \nabla \cdot (-\rho_w \rho_n (\bar{\lambda}_w \mathbf{K} \nabla \bar{p}_w + \bar{\lambda}_n \mathbf{K} \nabla \bar{p}_n) S'_w). \end{aligned} \quad (27)$$

4.2 Discrete linearized analysis

It is assumed that the upwinded discontinuous Galerkin weak form for the incompressible two-phase flow equations in Eqs. 1 - 2 is given by,

$$\begin{aligned} \mathcal{R}_{h,p}^{\text{upwind}}(\mathbf{u}; \mathbf{v}) = \mathcal{R}_{h,p}(\mathbf{u}; \mathbf{v}) \\ + \sum_{f \in \Gamma_I} \int_f \mathbf{g}(\mathbf{v}^\pm, \mathbf{u}^\pm, \nabla \mathbf{u}^\pm; \vec{n}^+) d\Gamma, \end{aligned} \quad (28)$$

where $\mathcal{R}_{h,p}(\mathbf{u}; \mathbf{v})$ is the standard DG weak form given by Eq. 10, and $\mathbf{g} = [g_w, g_n]^T$ represents an additional stabilization term that is yet to be determined. The complete form of $\mathcal{R}_{h,p}^{\text{upwind}}(\mathbf{u}; \mathbf{v})$ as applied to the incompressible wetting and non-wetting phase equations is given by Eqs. 69 and 70 respectively, in Appendix A.

As done previously for the continuous case, this DG weak form is then linearized about \bar{p}_n and \bar{S}_w , yielding the linearized weak form of the incompressible two-phase flow equations given by Eqs. 71 - 72. As detailed in Appendix A, a weighted sum of these linearized weak form equations produces the discrete weak form of the “pressure” equation (Eq. 73), and a weighted difference produces the discrete weak form of the “saturation” equation (Eq. 74).

4.3 Modification to discretization

The goal of this analysis is to find the appropriate stabilization terms, g_w and g_n , such that the linearized weak forms for the pressure and saturation equations given by Eq. 73 and Eq. 74 are consistent with the standard DG discretizations of the elliptic pressure equation in

Eq. 27 and the advection-diffusion equation for saturation in Eq. 23 respectively.

All of the terms in Eq. 73, except for the last integral involving g'_w and g'_n , are consistent with a centered (BR2) DG discretization of the elliptic pressure equation in Eq. 27. Assuming that a centered discretization is desired for the purely elliptic pressure equation, this implies that the last integral in Eq. 73 should be zero, producing the condition,

$$\rho_n g'_w = -\rho_w g'_n. \quad (29)$$

Next, consider the DG discretization of the linearized saturation equation in Eq. 24,

$$\begin{aligned} \sum_{\kappa \in \mathcal{T}_h} \int_{\kappa} v \frac{\partial S'_w}{\partial t} d\Omega - \sum_{\kappa \in \mathcal{T}_h} \int_{\kappa} \nabla v \cdot \vec{V} S'_w d\Omega \\ + \sum_{\kappa \in \mathcal{T}_h} \int_{\kappa} \nabla v \cdot \bar{\mathbf{D}} \nabla S'_w d\Omega \\ + \sum_{f \in \Gamma_I} \int_f \llbracket v \rrbracket \cdot \vec{F} d\Gamma \\ - \sum_{f \in \Gamma_I} \int_f \llbracket v \rrbracket \cdot \{ \bar{\mathbf{D}} (\nabla S'_w + \eta_f \vec{r}_S) \} d\Gamma \\ - \sum_{f \in \Gamma_I} \int_f \{ \bar{\mathbf{D}}^T \nabla v \} \cdot \llbracket S'_w \rrbracket d\Gamma = 0, \end{aligned} \quad (30)$$

where the numerical flux $\vec{F}(S'^+_w, S'^-_w; \vec{n}^+)$ is the exact upwind (Godunov) flux given by,

$$\vec{F} = \left\{ \vec{V} S'_w \right\} + \frac{1}{2} \left| \vec{V} \cdot \vec{n}^+ \right| \llbracket S'_w \rrbracket. \quad (31)$$

Multiplying Eq. 30 by $\rho_w \rho_n \phi(\bar{\lambda}_w + \bar{\lambda}_n)$ and comparing the result with Eq. 74 shows that the following condition needs to be satisfied on each face $f \in \Gamma_I$ in order for the two equations to match each other,

$$\begin{aligned} \int_f \rho_w \rho_n \phi(\bar{\lambda}_w + \bar{\lambda}_n) \llbracket v \rrbracket \cdot \vec{F} d\Gamma \\ = - \int_f \llbracket v \rrbracket \cdot \{ \rho_w \rho_n (\bar{\lambda}_w \mathbf{K} \nabla \bar{p}_w) S'_w \} d\Gamma \\ = - \int_f \llbracket v \rrbracket \cdot \{ \rho_w \rho_n (-\bar{\lambda}_w \bar{\lambda}_n \mathbf{K} \nabla \bar{p}_n) S'_w \} d\Gamma \\ + \int_f \rho_n \bar{\lambda}_n g'_w - \rho_w \bar{\lambda}_w g'_n d\Gamma. \end{aligned} \quad (32)$$

Substituting the expression for \vec{F} and canceling the average fluxes on both sides yields,

$$\begin{aligned} \int_f \llbracket v \rrbracket \cdot \frac{1}{2} \rho_w \rho_n \phi(\bar{\lambda}_w + \bar{\lambda}_n) \left| \vec{V} \cdot \vec{n}^+ \right| \llbracket S'_w \rrbracket d\Gamma \\ = \int_f \rho_n \bar{\lambda}_n g'_w - \rho_w \bar{\lambda}_w g'_n d\Gamma. \end{aligned} \quad (33)$$

Substituting the constraint in Eq. 29 into the right-hand side of the equation above and simplifying gives,

$$\int_f g'_w d\Gamma = \int_f \frac{1}{2} \llbracket v \rrbracket \cdot \rho_w \phi \left| \vec{V} \cdot \vec{n}^+ \right| \llbracket S'_w \rrbracket d\Gamma, \quad (34)$$

$$\int_f g'_n d\Gamma = - \int_f \frac{1}{2} \llbracket v \rrbracket \cdot \rho_n \phi \left| \vec{V} \cdot \vec{n}^+ \right| \llbracket S'_w \rrbracket d\Gamma. \quad (35)$$

Therefore, under the assumption of $\llbracket \bar{S}_w \rrbracket = 0$, the non-linear form of the stabilization terms required for upwinding can be inferred as,

$$\int_f g_w d\Gamma = \int_f \frac{1}{2} \llbracket v \rrbracket \cdot C_w(\mathbf{u}_{h,p}^\pm, \nabla \mathbf{u}_{h,p}^\pm; \vec{n}^+) \llbracket S_w \rrbracket d\Gamma, \quad (36)$$

$$\int_f g_n d\Gamma = - \int_f \frac{1}{2} \llbracket v \rrbracket \cdot C_n(\mathbf{u}_{h,p}^\pm, \nabla \mathbf{u}_{h,p}^\pm; \vec{n}^+) \llbracket S_w \rrbracket d\Gamma, \quad (37)$$

where $C_\alpha(\mathbf{u}_{h,p}^\pm, \nabla \mathbf{u}_{h,p}^\pm; \vec{n}^+)$ is given by,

$$C_\alpha = \max_{\mathbf{u}_{h,p} \in \{\mathbf{u}_{h,p}^+, \mathbf{u}_{h,p}^-\}} \left(\left| -\rho_\alpha \frac{\lambda_{ws} \lambda_n}{\lambda_w + \lambda_n} \mathbf{K} \nabla p_w^{\text{lifted}} \cdot \vec{n}^+ + \rho_\alpha \frac{\lambda_w \lambda_{ns}}{\lambda_w + \lambda_n} \mathbf{K} \nabla p_n^{\text{lifted}} \cdot \vec{n}^+ \right| \right), \quad (38)$$

for $\alpha \in \{w, n\}$ where the “lifted” pressure gradients are given by,

$$\begin{aligned} \nabla p_w^{\text{lifted}} &= \nabla p_n + \eta_f \vec{r}_p(\llbracket p_n \rrbracket) - p_{cs}(\nabla S_w + \eta_f \vec{r}_s(\llbracket S_w \rrbracket)), \\ \nabla p_n^{\text{lifted}} &= \nabla p_n + \eta_f \vec{r}_p(\llbracket p_n \rrbracket). \end{aligned} \quad (39)$$

In practical implementation, the maximum and absolute operators in Eq. 38 are replaced with smoother counterparts, which reduce discontinuities in the residual and thereby improve the nonlinear convergence behavior of the solver. This work uses the following smoothmax and smoothabs operators,

$$\text{smoothmax}(x, y) = \begin{cases} x + \frac{1}{\alpha} \log(1 + e^{\alpha(y-x)}), & \text{if } x > y, \\ y + \frac{1}{\alpha} \log(1 + e^{\alpha(x-y)}), & \text{otherwise,} \end{cases} \quad (40)$$

where $\alpha = 40$, and,

$$\text{smoothabs}(x) = \frac{x^2}{\text{sgn}(x)x + \epsilon}, \quad (41)$$

where $\epsilon = 10^{-3}$. Increasing α and decreasing ϵ cause the smoothmax and smoothabs functions to approach the regular maximum and absolute functions, respectively.

For the rest of this paper, the DG discretization of two-phase flow equations uses the modified weak form $\mathcal{R}_{h,p}^{\text{upwind}}(\mathbf{u}; \mathbf{v})$, with the stabilization terms derived in

Eqs. 36 - 37. Although the upwind stabilization terms g_w and g_n were derived under assumptions of incompressibility, they are also successfully used for slightly compressible flows later in this paper.

4.4 Numerical results

The semi-discrete form of the DG discretization of a linear PDE can be expressed compactly using the following system of ODEs,

$$\mathbf{M} \dot{\mathbf{u}} + \mathbf{A} \mathbf{u} = \mathbf{b}, \quad (42)$$

where $\mathbf{u}(t)$ is the discrete solution vector and the matrices \mathbf{M} and \mathbf{A} are formed from the temporal and spatial parts of the DG weak form respectively. The right-hand side vector $\mathbf{b}(t)$ usually contains forcing function and boundary condition data. Following the explanation given in Appendix B, the stability of the DG discretization of the linearized equations (Eqs. 71 - 72) can be evaluated numerically by forming the \mathbf{M} and \mathbf{A} matrices, and checking if the real components of their generalized eigenvalues ω are negative.

Consider a 1D incompressible two-phase flow problem in the domain $x \in [0, 100]$, with the following flow parameters,

$$\begin{aligned} \rho_w &= 62.4 \text{ lb/ft}^3, & \rho_n &= 52.1 \text{ lb/ft}^3, \\ \phi &= 0.3, & \mathbf{K} &= 200\mathbf{I} \text{ mD}, \\ k_{rw}(S_w) &= S_w^2, & k_{rn}(S_w) &= (1 - S_w)^2, \\ \mu_w &= 1 \text{ cP}, & \mu_n &= 2 \text{ cP}. \end{aligned}$$

Capillary effects are ignored in this problem (i.e. $p_c = 0$) in order to test for the worst-case of a purely hyperbolic saturation equation. The base solution about which the two-phase flow equations are linearized is chosen to be a linear pressure and constant saturation solution, which satisfies the nonlinear two-phase flow equations. The DG weak form given in Eqs. 71 - 72 is then used to discretize the linearized problem with the above parameters, on a 1D grid with 100 uniformly sized elements. Figures 2 and 3 show the generalized eigenvalues obtained from a piecewise constant (P0) DG discretization of the linearized two-phase flow equations with periodic boundary conditions, for two different base solutions. The black circles, which represent the eigenvalues of the standard BR2 discretization without the upwinding modification, lie on the imaginary axis showing that the system is only neutrally stable. This is similar to the result obtained when a linear advection equation is discretized with a central difference scheme. However, with the addition of the linearized upwinding terms g'_w and g'_n given in Eqs. 34

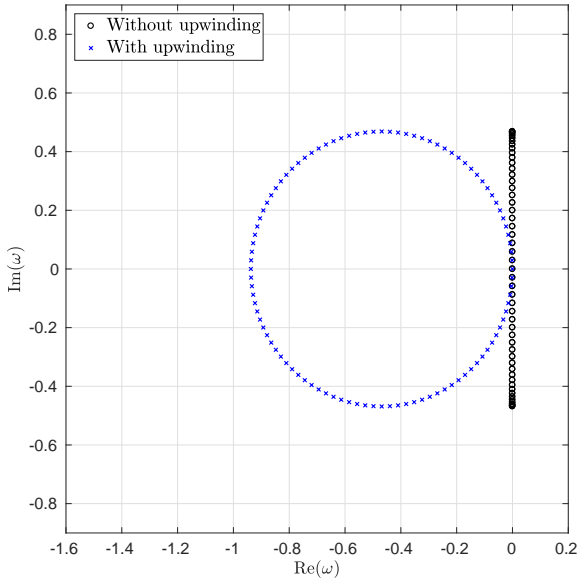


Fig. 2 Generalized eigenvalues of a DG P0 discretization of the linearized two-phase equations with periodic BCs, for a base solution with $\frac{d\bar{p}_n}{dx} = -0.25$, $\bar{S}_w = 0.2$.

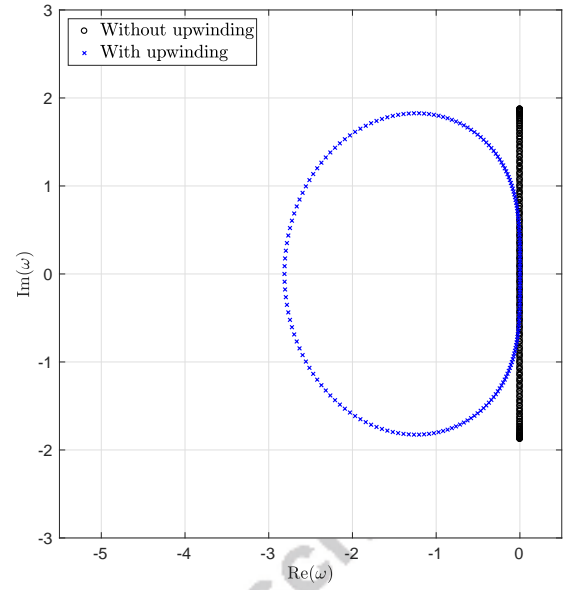


Fig. 4 Generalized eigenvalues of a DG P1 discretization of the linearized two-phase equations with periodic BCs, for a base solution with $\frac{d\bar{p}_n}{dx} = -0.25$, $\bar{S}_w = 0.2$.

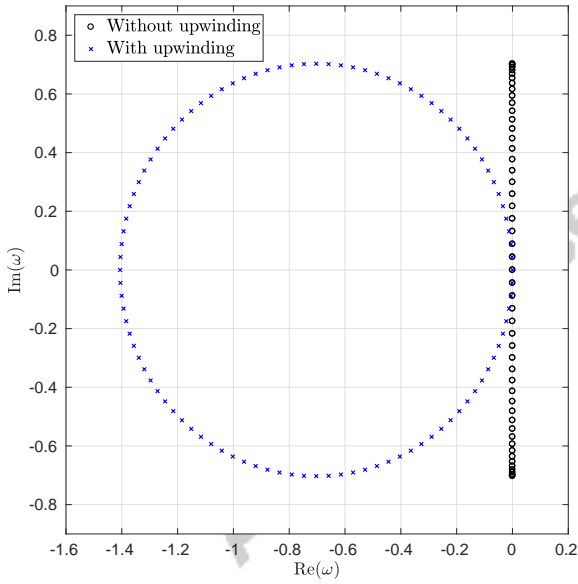


Fig. 3 Generalized eigenvalues of a DG P0 discretization of the linearized two-phase equations with periodic BCs, for a base solution with $\frac{d\bar{p}_n}{dx} = -0.25$, $\bar{S}_w = 0.5$.

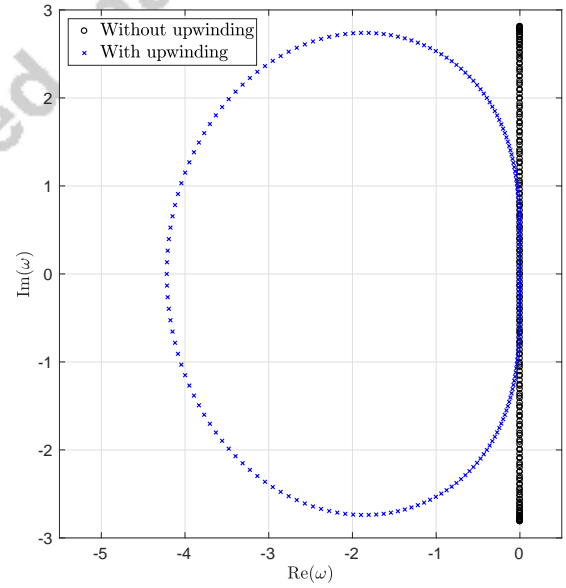


Fig. 5 Generalized eigenvalues of a DG P1 discretization of the linearized two-phase equations with periodic BCs, for a base solution with $\frac{d\bar{p}_n}{dx} = -0.25$, $\bar{S}_w = 0.5$.

- 35, the generalized eigenvalues move off the imaginary axis to form a circle in the stable left-half of the plane, as shown by the blue crosses. Figures 4 and 5 show the results for a piecewise linear (P1) DG discretization, where the upwinding terms stabilize the system in a similar manner. Note that the figures only show the finite eigenvalues corresponding to the saturation equation, since the eigenvalues of the elliptic pressure equation do not exist.

The effect of the nonlinear upwinding terms g_w and g_n (Eqs. 36 - 37) on the DG discretization of the nonlinear two-phase equations is investigated below, using the same test problem given above. Let $\mathbf{J}(\bar{\mathbf{u}}_{h,p})$ be the Jacobian matrix that arises from the DG discretization of the nonlinear two-phase equations (Eqs. 69 - 70), when evaluated about a discrete solution $\bar{\mathbf{u}}_{h,p}$. Further, let $\mathbf{J}_t(\bar{\mathbf{u}}_{h,p})$ and $\mathbf{J}_x(\bar{\mathbf{u}}_{h,p})$ be the temporal and spatial contributions to the Jacobian matrix, such that $\mathbf{J}(\bar{\mathbf{u}}_{h,p}) =$

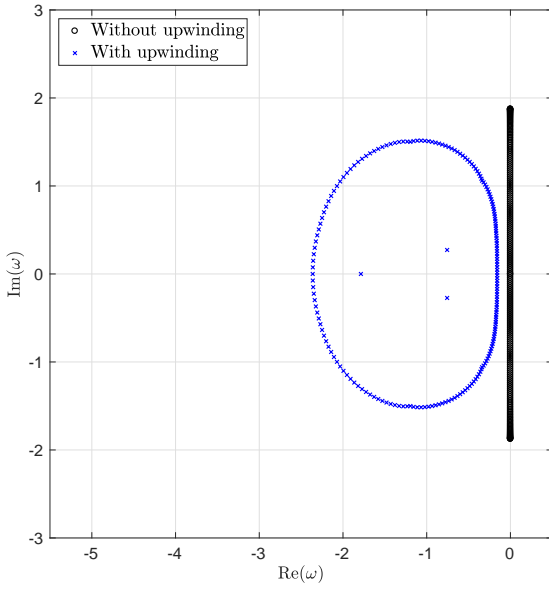


Fig. 6 Generalized eigenvalues of a DG P1 discretization of the linearized two-phase equations with Dirichlet BCs, for a base solution with $\frac{d\bar{p}_n}{dx} = -0.25, \bar{S}_w = 0.2$.

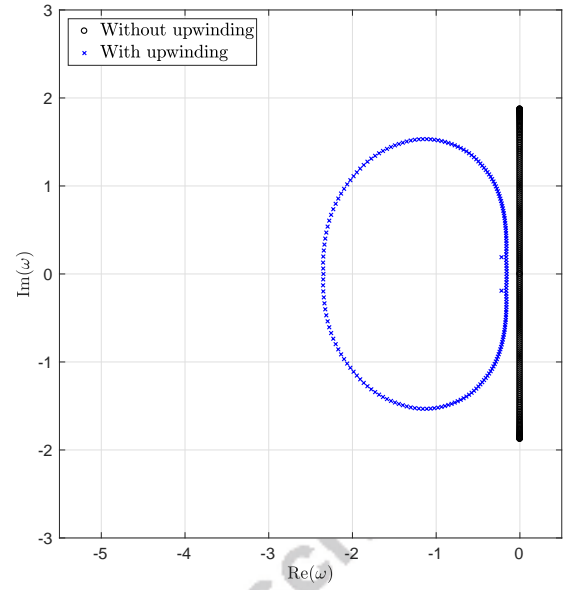


Fig. 8 Generalized eigenvalues of a DG P1 discretization of the nonlinear two-phase equations with Dirichlet BCs, evaluated at a P1 L^2 -projection of the base solution with $\frac{d\bar{p}_n}{dx} = -0.25, \bar{S}_w = 0.2$.

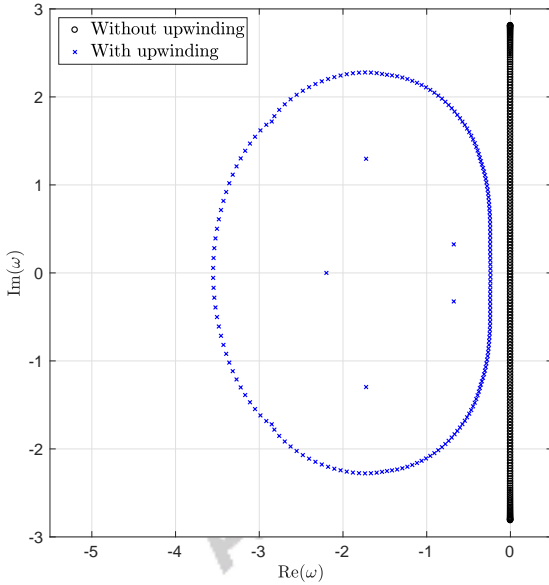


Fig. 7 Generalized eigenvalues of a DG P1 discretization of the linearized two-phase equations with Dirichlet BCs, for a base solution with $\frac{d\bar{p}_n}{dx} = -0.25, \bar{S}_w = 0.5$.

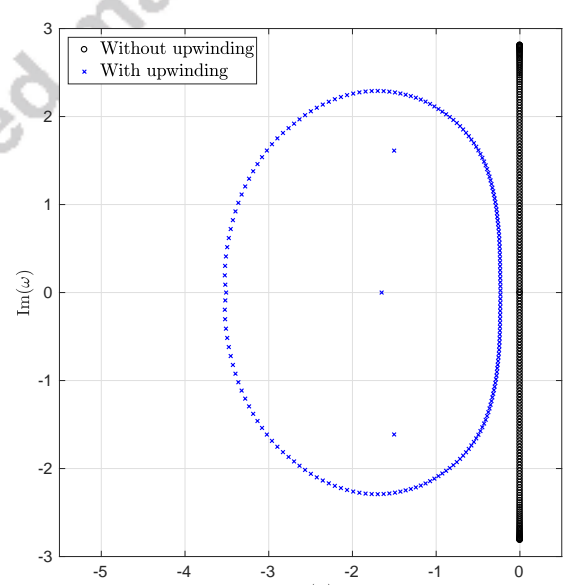


Fig. 9 Generalized eigenvalues of a DG P1 discretization of the nonlinear two-phase equations with Dirichlet BCs, evaluated at a P1 L^2 -projection of the base solution with $\frac{d\bar{p}_n}{dx} = -0.25, \bar{S}_w = 0.5$.

$\mathbf{J}_t(\bar{\mathbf{u}}_{h,p}) + \mathbf{J}_x(\bar{\mathbf{u}}_{h,p})$. Then, if the discrete solution $\bar{\mathbf{u}}_{h,p}$ is equal to the base solution about which the continuous equations are linearized (i.e. $\bar{\mathbf{u}}_{h,p} = [\bar{p}_n, \bar{S}_w]$), it is expected that the generalized eigenvalues of the problem $[\mathbf{J}_x \hat{\mathbf{u}}' = -\omega \mathbf{J}_t \hat{\mathbf{u}}']$ will be equal to those obtained for the linearized two-phase flow equations.

In order to test this, the \mathbf{J}_t and \mathbf{J}_x matrices from a P1 DG discretization of the nonlinear equations are evaluated at a discrete solution that is an L^2 -projection

of the base solution onto $\mathcal{V}_{h,p}$. A P1 DG discretization is used since a linear pressure and constant saturation solution can be represented exactly in the P1 discrete space. Figures 6 - 7 show the generalized eigenvalues obtained from a P1 discretization of the linearized two-phase equations with Dirichlet BCs for p'_n at both boundaries, and a Dirichlet BC for S'_w at the left boundary, for different base solutions. The addition of Dirich-

let BCs shifts the eigenvalues of the upwinded cases away from the origin. Figures 8 - 9 show the generalized eigenvalues obtained from a P1 discretization of the nonlinear two-phase flow equations, where the Jacobian matrices are evaluated at the same base solutions. The similarity of the eigenvalues in Figures 6 - 7 to those in Figures 8 - 9 confirms that the discretization of the nonlinear upwinding terms g_w and g_n behave as expected when linearized.

5 PDE-based artificial viscosity

High-order discretizations of hyperbolic conservation laws are known to produce spurious oscillations in the vicinity of solution discontinuities, which may also spread to regions of smooth flow and corrupt the accuracy of the solution globally. A key step towards mitigating these unphysical oscillations is to add dissipation, preferably in a controlled manner that does not affect smooth regions. In this section, we extend the PDE-based artificial viscosity method proposed by Barter and Darmofal [5] to high-order DG discretizations of two-phase flow problems.

5.1 Entropy-violating Buckley-Leverett solutions

This section presents DG solutions of the Buckley-Leverett equation to show that high-order discretizations may *converge* to entropy-violating solutions in the absence of physical or artificial diffusion.

Consider the Buckley-Leverett problem given below,

$$\frac{\partial}{\partial t} (\phi S_w) + \frac{\partial}{\partial x} (u_T f_w(S_w)) = 0, \quad (43)$$

$$S_w(x, 0) = 0.1, \quad x \in [0, L] \quad (44)$$

$$S_w(0, t) = 1, \quad t \in [0, T] \quad (45)$$

where the wetting phase saturation S_w is the dependent variable, porosity $\phi = 0.3$, and total velocity $u_T = 0.3$ ft/day. The fractional flow function $f_w(S_w)$ [4] is a non-linear, non-convex function defined as,

$$f_w(S_w) = \frac{S_w^2}{S_w^2 + \frac{\mu_w}{\mu_n}(1 - S_w)^2}. \quad (46)$$

The wetting-phase to non-wetting phase viscosity ratio $\frac{\mu_w}{\mu_n}$ is assumed to be equal to 0.5, and the relative permeabilities are modeled as quadratic functions. The domain length L is equal to 50 ft, and the final time T is 25 days.

Figures 10 - 12 show piecewise constant (P0) DG solutions to the above problem, as solved on a structured mesh with 100 line elements. The discrete solutions in Figure 10 and Figure 11 use BDF1 and BDF2

time-marching schemes respectively, each with constant time-steps of $\Delta t = 0.1$ days. Figure 12 uses a BDF1 scheme with smaller time-steps of $\Delta t = 0.01$ days. The solid lines represent the discrete solutions at different times, and the dashed lines represent that analytic Buckley-Leverett solution. The discrete solutions correctly produce a combined rarefaction-shock wave propagating through the domain, but the saturation front is clearly diffused as a result of numerical dissipation. The smearing of the front is lesser in Figures 11 and 12 compared to Figure 10, due to the greater temporal accuracy.

Similarly, Figures 13 - 15 show piecewise linear (P1) DG solutions for the same problem, using BDF1 and BDF2 time-marching schemes. The discrete solutions in Figures 13 and 14 use $\Delta t = 0.1$ days, whereas Figure 15 uses $\Delta t = 0.01$ days. The saturation front in the P1-BDF1 solution is significantly less diffused compared to the P0 solutions, and agrees well with the analytic solution. However, the P1-BDF2 method converges to a solution that has an incorrect front speed, an incorrect saturation jump across the front, and some unphysical oscillations. The flat solution profile downstream of the front is also different from the analytic solution. The solution value in this flat region corresponds to a characteristic speed that is much slower than the speed of the shock. This residual-converged P1 solution is therefore clearly entropy violating in the sense of Oleinik's entropy condition [35], since it contains characteristics that emanate out of the shock on the downstream side. It should also be noted that the P1-BDF2 DG method does not converge to an entropy satisfying solution even with further mesh resolution and time-step refinement, unless dissipation is added explicitly (e.g. through capillary effects). Furthermore, the P1-BDF1 DG solution also develops oscillations and converges to an entropy-violating solution as the time-step size is reduced, as seen in Figure 15. In contrast, the P0 DG solutions remain physical with time-step refinement, as seen in Figure 12.

These results show that high-order spatial discretizations of the Buckley-Leverett equation require a stabilization mechanism that ensures convergence to entropy-satisfying solutions. Further, considering that the Buckley-Leverett equation is a simplified model for the saturation transport in the two-phase flow equations, it is reasonable to assume that high-order discretizations of the two-phase flow equations may also converge to entropy-violating solutions, especially in the limit of vanishing physical diffusion. This therefore also motivates the development of a discontinuity-capturing method for the two-phase flow equations.

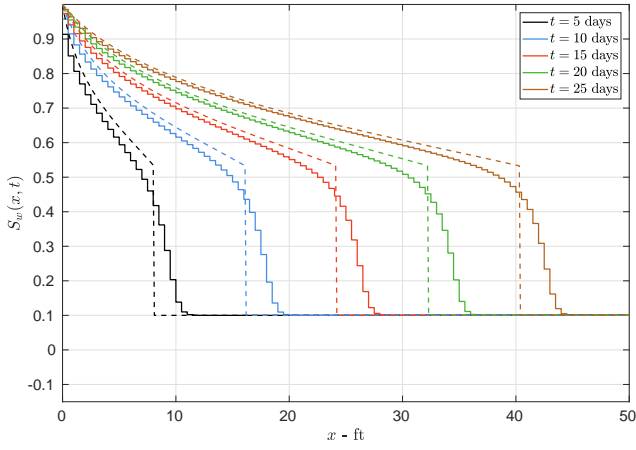


Fig. 10 Comparison of the P0 DG solution using BDF1 time-marching with $\Delta t = 0.1$ days (solid lines) against the analytic solution (dashed lines) at different times.

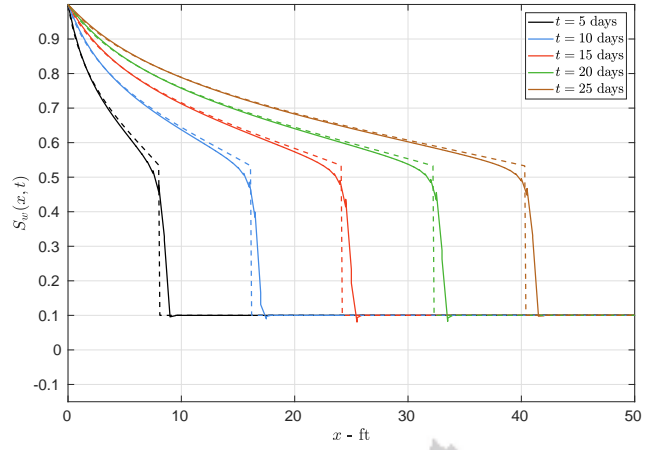


Fig. 13 Comparison of the P1 DG solution using BDF1 time-marching with $\Delta t = 0.1$ days (solid lines) against the analytic solution (dashed lines) at different times.

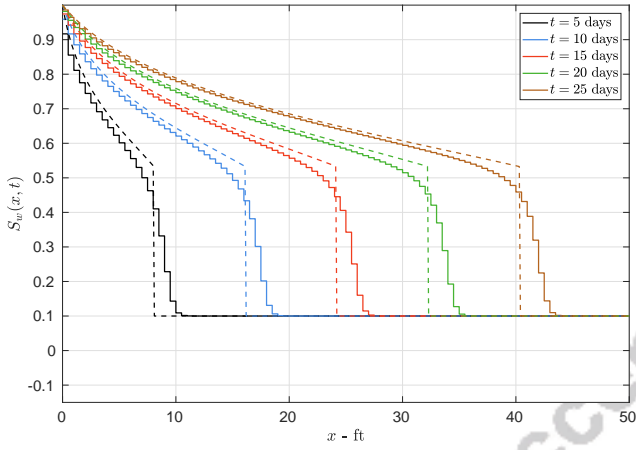


Fig. 11 Comparison of the P0 DG solution using BDF2 time-marching with $\Delta t = 0.1$ days (solid lines) against the analytic solution (dashed lines) at different times.

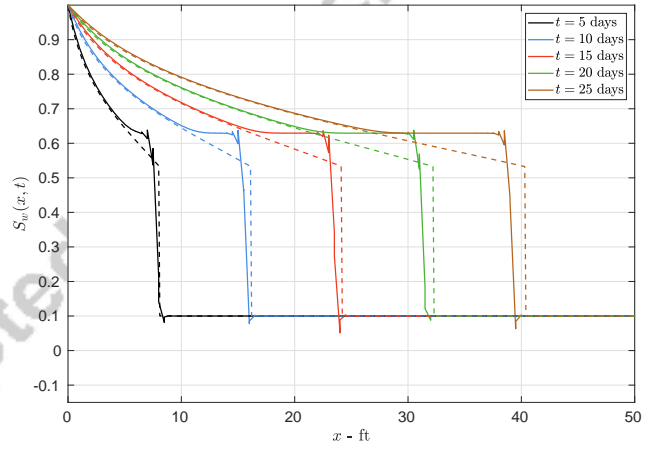


Fig. 14 Comparison of the P1 DG solution using BDF2 time-marching with $\Delta t = 0.1$ days (solid lines) against the analytic solution (dashed lines) at different times.

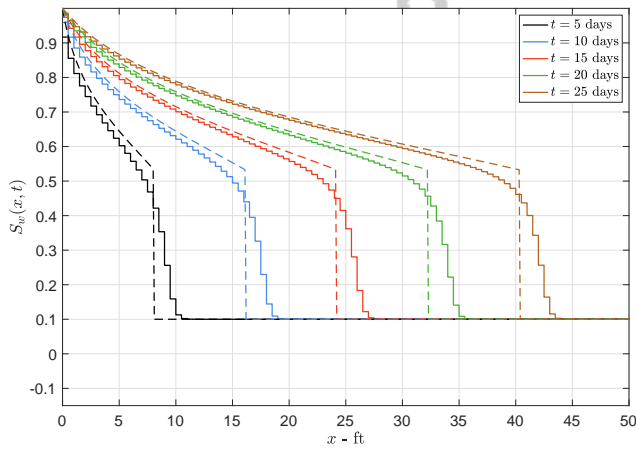


Fig. 12 Comparison of the P0 DG solution using BDF1 time-marching with $\Delta t = 0.01$ days (solid lines) against the analytic solution (dashed lines) at different times.

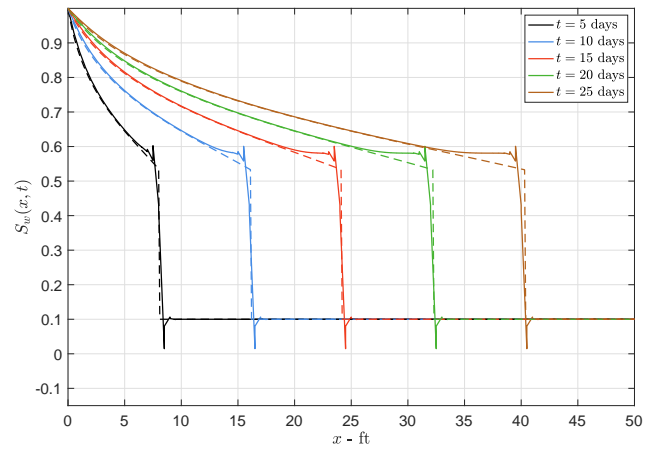


Fig. 15 Comparison of the P1 DG solution using BDF1 time-marching with $\Delta t = 0.01$ days (solid lines) against the analytic solution (dashed lines) at different times.

5.2 Artificial viscosity PDE

This work uses a modified version of the PDE-based artificial viscosity method introduced by Barter and Darmofal [5], where the distribution of artificial viscosity is governed by a reaction-diffusion equation. The reaction term generates artificial viscosity in regions with solution discontinuities, as dictated by a “shock sensor”, and the diffusion term helps to smooth the generated artificial viscosity. This auxiliary PDE is then solved together with the primary equations (e.g. Buckley-Leverett, two-phase flow) in a coupled manner.

In Barter’s original formulation, the artificial viscosity equation is cast as an unsteady equation with a time derivative term, with a time scale chosen such that the artificial viscosity evolves at least as fast as the primary equations. However, most reservoir flow problems, such as the two-phase flows considered in this work, are driven by an underlying pressure equation that is elliptic or near-elliptic. Hence, it seems reasonable to modify the artificial viscosity equation to be elliptic as well, thereby eliminating any lag between the need for artificial viscosity and the production of artificial viscosity. Therefore in this work, the temporal term in Barter’s original equation is omitted, and an elliptic artificial viscosity smoothing is investigated.

The artificial viscosity variable, $\nu(\vec{x}, t)$, is assumed to be governed by the scalar reaction-diffusion PDE given below,

$$-\nabla \cdot (C_1 \mathbf{H}^2 \nabla \nu) + \nu = f_{\text{switch}}(\xi(s)) \nu_{\text{max}}, \quad (47)$$

where $\mathbf{H}(\vec{x})$ is a symmetric and positive definite generalized length scale tensor that describes the spatial size of the local mesh elements, and C_1 is a constant that roughly determines the number of mesh elements over which artificial viscosity is diffused. In this work, C_1 is set to 3. Although Barter’s original formulation uses axis-aligned bounding boxes to measure the local mesh sizes, the formulation presented here uses Yano’s modification to the length scale calculation [55], where the generalized length scale tensor is computed from the Riemannian metric tensor as $\mathbf{H}(\vec{x}) = \mathcal{M}^{-1/2}(\vec{x})$. The Riemannian metric tensor captures information about the size and anisotropy of mesh elements, and is computed using the Jacobian of the transformation from a unit reference element to a given mesh element. The use of tensor-based length scales instead of vector-based length scales has been shown to improve the resolution of shocks on meshes with arbitrarily oriented, highly anisotropic elements [55].

Since straight-sided mesh elements are used in this work, the generalized length scale tensor field is represented using a discontinuous, piecewise constant (P0)

solution basis, where the length scale tensor value in an element κ is computed as the inverse matrix square root of the elemental metric tensor of κ . This produces a length scale tensor field that is discontinuous between elements for unstructured meshes. Alternatively, the length scale tensor field may also be represented using a continuous, piecewise linear (P1) solution basis, where the \mathbf{H} value at a mesh vertex is computed from a log-Euclidian average of the elemental metric tensors of the elements around that vertex. However, this approach tends to produce more negative artificial viscosity values on unstructured meshes compared to the piecewise constant representation, and is therefore not used in this work.

The production of artificial viscosity is driven by the forcing term on the right-hand side of Eq. 47, which becomes non-zero in the vicinity of solution discontinuities. The function $f_{\text{switch}}(\cdot) : \mathbb{R} \rightarrow (0, 1)$ is a non-linear, monotone switch such that $f_{\text{switch}}(0) \approx 0$ and $f_{\text{switch}}(1) \approx 1$. This work uses the following definition for the switch,

$$f_{\text{switch}}(x) = x + \frac{1}{\alpha} \log \left(\frac{1 + e^{-\alpha x}}{1 + e^{-\alpha(1-x)}} \right), \quad (48)$$

with $\alpha = 10$. This switch operates on a cell discontinuity sensor s , which quantifies the magnitude of solution discontinuities present around a given mesh element. This cell discontinuity sensor s is then also filtered, via $\xi(s)$, to ignore small discontinuities (i.e. smooth regions) and to cap the discontinuity level at which artificial viscosity production is maximized.

In this paper, s is represented using a scalar, piecewise constant (P0) DG solution, and is computed by solving the following linear local problem on each element κ ,

$$\frac{1}{|\kappa|} \int_{\kappa} v s \, d\Omega = \sum_{f \in \partial\kappa \cap \Gamma_I} \frac{1}{N_{\text{face}} |f|} \int_f v^+ g(\mathbf{u}^+, \mathbf{u}^-) \, d\Gamma, \quad \forall v \in V_{h,(p=0)}, \quad (49)$$

where $|\kappa|$ and N_{face} represent the volume and the number of faces of element κ , respectively. The area of an interior face f is denoted by $|f|$, and $g(\mathbf{u}^+, \mathbf{u}^-)$ is a scalar quantity used to detect a shock, which depends on the primary solution variables on either side of a face. Solving Eq. 49 on an element κ causes the value of the cell sensor s in that element to roughly equal the average value of g over the faces of κ . Since this work is concerned with detecting and stabilizing oscillations in the saturation solution, g is defined to be the absolute value of the jump in saturation across a face,

$$g(\mathbf{u}^+, \mathbf{u}^-) = |S_w^+ - S_w^-|. \quad (50)$$

The local problem in Eq. 49 is a modified version of Barter's jump indicator [5] that also extends to higher-order polynomial representations of the sensor variable. Solving Eq. 49 repeatedly for all elements in the mesh causes interior face integrals to be computed twice. Hence, for computational efficiency, Eq. 49 is summed over all elements in the mesh and re-arranged to produce the following alternate weak form,

$$\sum_{\kappa \in \mathcal{T}_h} \int_{\kappa} v s \, d\Omega = \sum_{f \in \Gamma_I} \int_f \left(\frac{|\kappa^+| v^+}{N_{\text{face}}^+ |f|} + \frac{|\kappa^-| v^-}{N_{\text{face}}^- |f|} \right) g(\mathbf{u}^+, \mathbf{u}^-) \, d\Gamma, \quad \forall v \in V_{h,(p=0)}, \quad (51)$$

where N_{face}^+ and N_{face}^- represent the number of faces of κ^+ and κ^- respectively. Assuming the mass matrix inverse of each element is computed and stored beforehand, this formulation allows the cell sensor s to be computed efficiently through accumulation, using only a single loop over the interior faces of the mesh. Higher-order representations of the cell sensor s can be easily obtained through this formulation by changing the order of the polynomial basis used for v and s in Eq. 51, but the effects of doing so are not considered in this paper.

Once the cell discontinuity sensor s is computed, it is filtered through $\xi(s)$ as follows,

$$\xi(s) = \frac{\log_{10}(|s| + \epsilon) - \log_{10}(s_{\min})}{\log_{10}(s_{\max}) - \log_{10}(s_{\min})}, \quad (52)$$

where s_{\min} and s_{\max} represent thresholds for the addition of artificial viscosity. When $\xi(s)$ is fed through the nonlinear activation function $f_{\text{switch}}(\cdot)$, regions with sensor values lower than s_{\min} do not produce any artificial viscosity, whereas regions with sensor values greater than s_{\max} produce the maximum amount of artificial viscosity. In this work, $s_{\min} = 10^{-3}$, $s_{\max} = 10^{-1}$ and $\epsilon = 10^{-16}$.

The last component of the artificial viscosity PDE is ν_{\max} , which represents the maximum amount of artificial viscosity that is added to the primary equations. As proposed by Persson and Peraire in [44], ν_{\max} needs to be $\mathcal{O}(h/p)$ to allow for sub-cell shock resolution, where h is the local mesh size and p is the polynomial order of the solution. The form of ν_{\max} used in this work is based on a multi-dimensional and higher-order extension of the grid Péclet number, given by,

$$\nu_{\max}(\mathbf{u}) = \frac{\sqrt{\bar{v}^T \mathbf{H}^2 \bar{v}}}{2p}, \quad \text{for } p > 0, \quad (53)$$

where $\mathbf{H}(\vec{x})$ is the generalized spatial length scale tensor from before, $\bar{v}(\mathbf{u})$ is a problem-dependent characteristic

velocity, and p is the solution order. The maximum artificial viscosity is designed to achieve a local grid Péclet number of $\text{Pe} = 2$, inspired from the stability theory of second-order finite difference schemes for 1D linear advection-diffusion problems.

The boundary conditions of the artificial viscosity PDE were specified to be of the radiation-type (i.e. Robin) by Barter and Darmofal [5], where the flux of ν is proportional to the difference between the boundary value and an ambient viscosity value (ν_{∞}), multiplied by a local length scale. Since it is possible for a shock or discontinuity to leave the domain at an arbitrary angle to the boundary, homogeneous Dirichlet ($\nu = 0$) or Neumann ($\frac{\partial \nu}{\partial \vec{n}} = 0$) BCs are not appropriate. The strong form of the Robin BC used in this work is given by,

$$-(C_1 \mathbf{H}^2 \nabla \nu) \cdot \vec{n} = \sqrt{C_1} (\vec{n}^T \mathbf{H} \vec{n}) (\nu - \nu_{\infty}), \quad (54)$$

where \vec{n} is the outward unit normal vector of the spatial boundary, and the ambient viscosity value is set to zero ($\nu_{\infty} = 0$). Since the term on the left-hand side of Eq. 54 is exactly the diffusive flux of the artificial viscosity PDE, this BC is discretized by setting the discrete boundary flux equal to the term on the right-hand side, where ν is evaluated from the interior of the domain ($\nu^B = \nu^+$).

5.3 Artificial viscosity for Buckley-Leverett

This section presents results for the Buckley-Leverett problem considered previously in Section 5.1, but now modified with the proposed artificial viscosity term to help mitigate unphysical oscillations that may occur when high-order discretizations are used. The original Buckley-Leverett equation is modified as follows,

$$\frac{\partial}{\partial t} (\phi S_w) + \frac{\partial}{\partial x} (u_T f_w(S_w)) = \frac{\partial}{\partial x} \left(\phi \tilde{\nu} \frac{\partial S_w}{\partial x} \right), \quad (55)$$

where,

$$\tilde{\nu}(\nu) = \text{smoothmax}(\nu, 0), \quad (56)$$

and the artificial viscosity $\nu(x, t)$ is an auxiliary variable that is governed by the artificial viscosity PDE. The primary state vector is augmented to include the artificial viscosity (i.e. $\mathbf{u} = [S_w, \nu]^T$) and Eq. 55 is solved in a coupled manner with the artificial viscosity PDE presented in the previous subsection. The artificial viscosity variable is passed through a smoothmax function, as given by Eq. 56, to ensure that the viscosity added to the Buckley-Leverett equation is always positive, since it is possible for a piecewise polynomial representation of ν to produce negative values, especially on highly

anisotropic elements. The characteristic velocity of the Buckley-Leverett equation required for the calculation of ν_{\max} is given by,

$$\vec{v} = \frac{u_T}{\phi} \frac{df_w}{dS_w}, \quad (57)$$

where $f_w(S_w)$ is the fractional flow function given by Eq. 46. The coupled system of equations is then solved for $\mathbf{u}(x, t)$ using a piecewise linear (P1) DG method with BDF1 and BDF2 time-marching schemes as before.

Figures 16 and 17 show the evolution of the P1 DG solutions obtained with the BDF1 and BDF2 time-marching schemes respectively. The dashed lines on each plot show the analytic Buckley-Leverett solution at different times. Comparing these saturation solutions with Figure 14 shows that the addition of artificial viscosity enables the P1 BDF2 scheme to converge to the correct physical solution, while also having less dissipation (and therefore sharper fronts) compared to the P0 BDF2 result. The artificial viscosity solutions plotted at the bottom of each figure clearly show how the peak value of ν closely tracks the saturation front as it moves across the domain.

5.4 Artificial viscosity for two-phase flow

This section describes a method for adding artificial viscosity to the two-phase flow equations in mass conservation form, in order to mitigate Gibbs oscillations in the saturation solution. Since the hyperbolic nature of the two-phase flow equations originates from the underlying saturation transport equation, it is important to add artificial viscosity in a manner that stabilizes the saturation behavior, while minimizing its effect on the elliptic pressure behavior for accuracy.

Intuitively, a capillary pressure based (i.e. physics-based) artificial viscosity model seems a reasonable choice, where any existing capillary pressure is augmented with an artificial viscosity of the same form, i.e. by substituting $(p_{cs} - \nu)$ for p_{cs} in Eq. 1. Linearizing the two-phase flow equations with this form of artificial viscosity, as done previously in Section 4.1, shows that the diffusion coefficient of the linearized saturation equation is,

$$\bar{D} = \frac{\bar{\lambda}_w \bar{\lambda}_n}{\phi(\bar{\lambda}_w + \bar{\lambda}_n)} (\nu - \bar{p}_{cs}) \mathbf{K}, \quad (58)$$

where all quantities with an overbar ($\bar{\cdot}$) are evaluated at the base state. Note that \bar{p}_{cs} is non-positive, so the diffusion coefficient \bar{D} is non-negative as long as the artificial viscosity ν is non-negative. However, the presence of a product of relative mobilities in the numerator

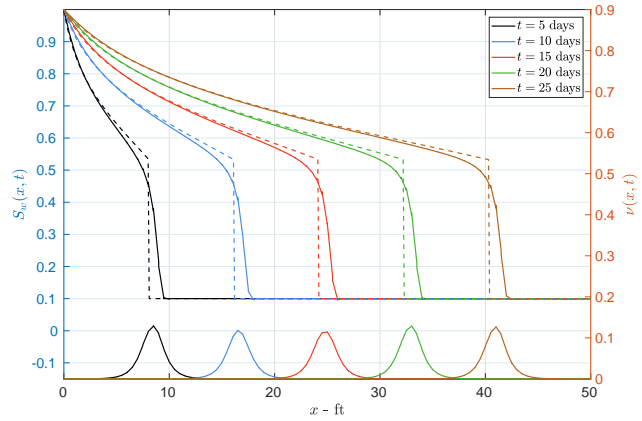


Fig. 16 Comparison of the P1 DG S_w solution (solid lines) with the analytic solution (dashed lines) at different times, with the ν solution plotted at the bottom. These solutions were obtained using the BDF1 time-marching scheme.

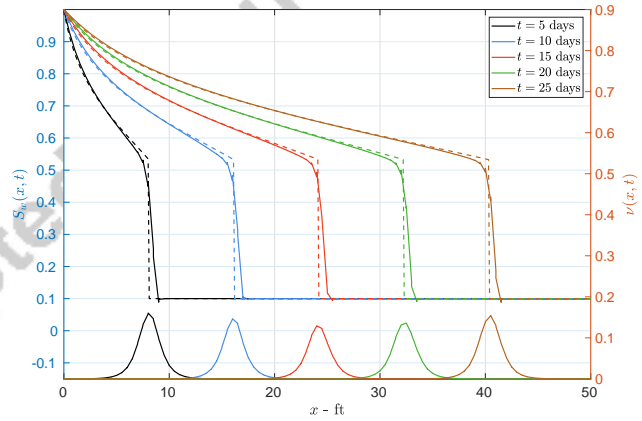


Fig. 17 Comparison of the P1 DG S_w solution (solid lines) with the analytic solution (dashed lines) at different times, with the ν solution plotted at the bottom. These solutions were obtained using the BDF2 time-marching scheme.

of Eq. 58 implies that \bar{D} vanishes in the limit of $\bar{S}_w \rightarrow 0$ or $\bar{S}_w \rightarrow 1$, regardless of the values of ν and \bar{p}_{cs} . Figure 18 shows examples of how the mobility-dependent term in Eq. 58 varies with S_w , for different phase viscosity ratios. As a result, this form of artificial viscosity is unable to add dissipation and stabilize regions with saturation values close to zero or one, which unfortunately, are also the regions that are most likely to give rise to unphysical saturations.

Therefore in this work, we propose a slightly more contrived artificial viscosity formulation for the two-phase flow equations, which is capable of adding dissipation in a more uniform manner for all values of saturation. Consider the following form of the two-phase

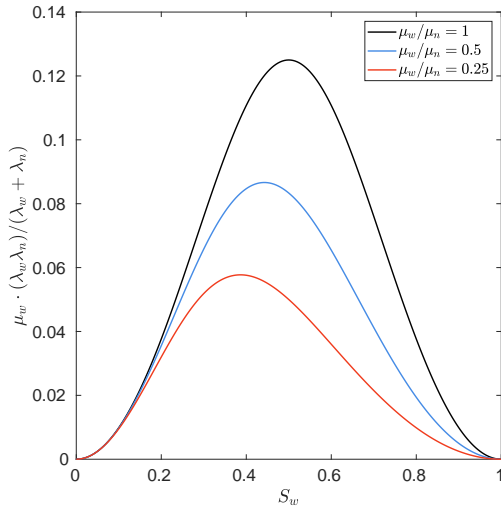


Fig. 18 Plot of $\mu_w \frac{\lambda_w \lambda_n}{\lambda_w + \lambda_n}$ vs. S_w using quadratic relative permeability functions, for different phase viscosity ratios.

flow equations modified with artificial viscosity,

$$\frac{\partial}{\partial t} (\rho_w \phi S_w) - \nabla \cdot (\rho_w \lambda_w \mathbf{K} \nabla p_w + \rho_w \nu \nabla S_w) = 0, \quad (59)$$

$$\frac{\partial}{\partial t} (\rho_n \phi (1 - S_w)) - \nabla \cdot (\rho_n \lambda_n \mathbf{K} \nabla p_n - \rho_n \nu \nabla S_w) = 0, \quad (60)$$

where the artificial viscosity $\nu \geq 0$. Unlike for the capillary pressure-based artificial viscosity formulation described earlier, taking the weighted sum of the augmented equations, $\rho_n \times (\text{Eq. 59}) + \rho_w \times (\text{Eq. 60})$, in the incompressible limit causes the artificial viscosity terms to cancel each other out. This shows that the addition of this form of artificial viscosity does not affect the underlying pressure equation. Furthermore, the diffusion coefficient of the corresponding linearized saturation equation is,

$$\bar{\mathbf{D}} = -\frac{\bar{\lambda}_w \bar{\lambda}_n}{\phi(\bar{\lambda}_w + \bar{\lambda}_n)} \bar{p}_{cs} \mathbf{K} + \frac{\nu}{\phi} \mathbf{I}, \quad (61)$$

which adds artificial dissipation uniformly across all saturation values.

In order to complete the description of the artificial viscosity formulation, a definition of the maximum artificial viscosity ν_{\max} is also required. In this work, ν_{\max} is defined such that when $\nu = \nu_{\max}$ and capillary effects are ignored (i.e. $p_c = 0$), the linearized saturation equation has a grid Péclet number equal to $\text{Pe} = 2$. Using the multi-dimensional and high-order extension of the grid Péclet number for the linearized saturation equation yields the following expression for ν_{\max} ,

$$\frac{\nu_{\max}}{\phi} = \frac{\sqrt{\vec{V}^T \mathbf{H}^2 \vec{V}}}{2p}, \quad (62)$$

where \vec{V} is the saturation advection velocity given in Eq. 25. However, the presence of relative mobilities ($\bar{\lambda}_w, \bar{\lambda}_n$) and their derivatives ($\bar{\lambda}_{wS}, \bar{\lambda}_{nS}$) in the expression of \vec{V} makes the expression for ν_{\max} , and consequently also the artificial viscosity PDE, highly nonlinear with respect to saturation. This nonlinearity is alleviated for better discretization robustness, at the expense of using a more conservative velocity estimate, which does not contain the nonlinear relative permeability functions. Hence, the saturation advection velocity \vec{V} is replaced with \vec{V}_{\max} given below,

$$\vec{V}_{\max} = \arg \max_{\vec{V}_\alpha \in \{\vec{V}_w, \vec{V}_n\}} (|\vec{V}_\alpha|), \quad (63)$$

where \vec{V}_α represents the seepage velocity of phase α ,

$$\vec{V}_\alpha = -\frac{1}{\phi} \frac{\mathbf{K} \nabla p_\alpha}{\mu_\alpha}. \quad (64)$$

The physical significance of \vec{V}_{\max} above is that it represents the seepage velocity of the faster moving phase. For a problem with no capillary effects (i.e. $p_w = p_n$), \vec{V}_{\max} is always the seepage velocity of the less viscous phase.

The final form of the two-phase flow equations augmented with the artificial viscosity PDE is given below,

$$\begin{aligned} \frac{\partial}{\partial t} (\rho_w \phi S_w) - \nabla \cdot (\rho_w \lambda_w \mathbf{K} \nabla p_w + \rho_w \tilde{\nu} \nabla S_w) &= 0, \\ \frac{\partial}{\partial t} (\rho_n \phi (1 - S_w)) - \nabla \cdot (\rho_n \lambda_n \mathbf{K} \nabla p_n - \rho_n \tilde{\nu} \nabla S_w) &= 0, \\ -\nabla \cdot (C_1 \mathbf{H}^2 \nabla \nu) + \nu &= f_{\text{switch}}(\xi(s)) \nu_{\max}, \end{aligned} \quad (65)$$

where $\mathbf{u} = [p_n, S_w, \nu]^T$ is the augmented state vector, and $\tilde{\nu}$ represents the value of viscosity obtained after passing ν through the smoothmax function given in Eq. 56. As before, $\tilde{\nu}$ ensures that the artificial dissipation added to the primary equations is positive. Numerical results obtained using this formulation are presented in the next section.

6 Application

This section presents numerical results for a slightly compressible two-phase flow problem in a two-dimensional heterogeneous reservoir. This problem is challenging for high-order discretizations due to the presence of a discontinuous rock permeability field and the absence of physical diffusion (zero capillary effects), and therefore requires the use of artificial viscosity to robustly converge the solutions. Output predictions from a high-order DG method with artificial viscosity are compared to those from a conventional finite volume method (without artificial viscosity) for computational efficiency.

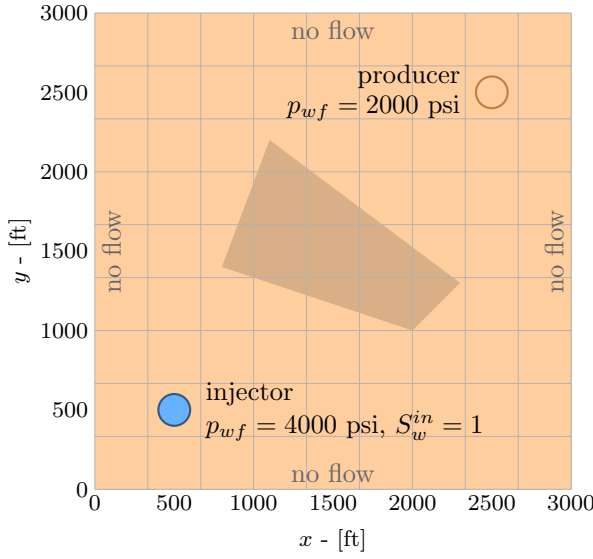


Fig. 19 Schematic of heterogeneous reservoir.

6.1 Test problem

The problem considered in this section involves a slightly compressible water-oil system that is driven by a two-spot well configuration in a square, heterogeneous reservoir. The spatial domain is given by $\Omega_s = [0, L] \times [0, L]$, where $L = 3000$ ft. The depth of the reservoir, L_z , is assumed to be constant and is not explicitly modeled, thereby resulting in a 2D problem. The schematic in Figure 19 shows the locations of the injection and production wells, at coordinates (500, 500) ft and (2500, 2500) ft, with fixed bottom-hole pressures of 4000 psi and 2000 psi respectively. The darker region in the figure represents the quadrilateral heterogeneity in the absolute rock permeability field, where the permeability is 100 times smaller compared to the rest of the reservoir, and thus manifests as a barrier to the flow between the wells. The corners of the quadrilateral block are at spatial coordinates (800, 1400), (2000, 1000), (2300, 1300) and (1100, 2200) ft. The permeability changes discontinuously across the boundary of the quadrilateral, representing an abrupt change in the geology.

The relevant constitutive relationships and numerical constants are,

$$\begin{aligned} \rho_\alpha &= \rho_{\alpha_{\text{ref}}} e^{c_\alpha(p_\alpha - p_{\text{ref}})} & \text{for } \alpha \in \{w, n\}, \\ \phi &= \phi_{\text{ref}} e^{c_\phi(p_n - p_{\text{ref}})}, \\ k_{r\alpha} &= S_\alpha^2, & \text{for } \alpha \in \{w, n\} \\ p_c &= 0, \end{aligned}$$

where,

$$\begin{aligned} \phi_{\text{ref}} &= 0.3, & p_{\text{ref}} &= 14.7 \text{ psi}, \\ \rho_{w_{\text{ref}}} &= 62.4 \text{ lb/ft}^3, & \rho_{n_{\text{ref}}} &= 52.1 \text{ lb/ft}^3, \\ c_w &= 5 \times 10^{-6} \text{ psi}^{-1}, & c_n &= 1.5 \times 10^{-5} \text{ psi}^{-1}, \\ c_\phi &= 3 \times 10^{-6} \text{ psi}^{-1}, & r_w &= 2 \text{ inches}, \\ \mathbf{K}_{\text{ref}} &= 200 \text{ I mD}, & \mathbf{K}_{\text{block}} &= 2 \text{ I mD}, \\ \mu_w &= 1 \text{ cP}, & \mu_n &= 2 \text{ cP}. \end{aligned}$$

The boundary conditions for this problem are no flow conditions across all four boundaries of the domain, and the initial conditions are $p_n(\vec{x}, 0) = 3000$ psi and $S_w(\vec{x}, 0) = 0.1$. The objective of the problem is to accurately predict the oil recovery factor given by,

$$J = \frac{V_{n_{\text{out}}}}{V_{OIP}}, \quad (66)$$

where $V_{n_{\text{out}}}$ is the total volume of oil extracted from the production well over a period of $T = 4000$ days, and V_{OIP} is the total volume of oil-in-place at $t = 0$, which are defined as follows,

$$V_{n_{\text{out}}} = L_z \int_0^T \int_0^L \int_0^L -q_n \, dx \, dy \, dt, \quad (67)$$

$$\begin{aligned} V_{OIP} &= L_z \int_0^L \int_0^L \phi \cdot (1 - S_w(x, y, 0)) \, dx \, dy \\ &= 2.4519 \times 10^6 L_z \text{ ft}^3. \end{aligned} \quad (68)$$

6.2 Numerical results

The two-phase flow problem described above is solved using the different discretizations listed below, and their output predictions are compared for accuracy and efficiency.

1. Finite volume (FV) method using a two-point flux approximation with upstream mobility weighting, and a backward Euler (BDF1) time-marching scheme. This scheme is first-order accurate in both space and time.
2. Piecewise linear (P1) DG method using a second order backward differentiation formula (BDF2) time-marching scheme. This scheme is second-order accurate in both space and time.
3. Piecewise quadratic (P2) DG method using a third order backward differentiation formula (BDF3) time-marching scheme. This scheme is third-order accurate in both space and time.

The first-order finite volume method does not require artificial viscosity since it does not introduce spurious oscillations, and therefore solves the two-phase

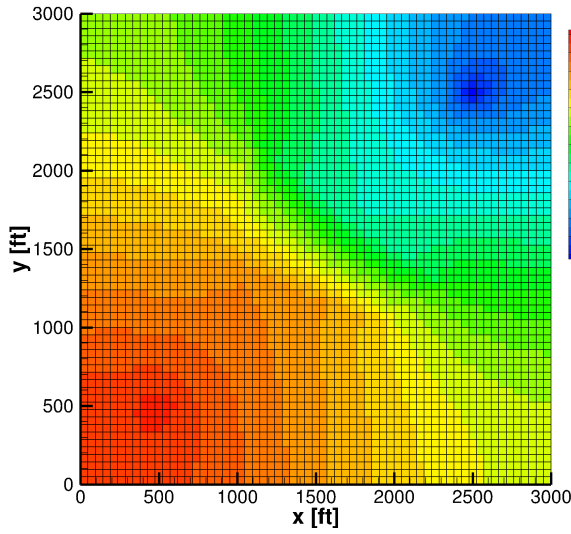


Fig. 20 Plot of p_n solution from the FV method with BDF1 on a 63×63 grid with 500 timesteps ($\Delta t = 8$ days), at $t = 4000$ days.

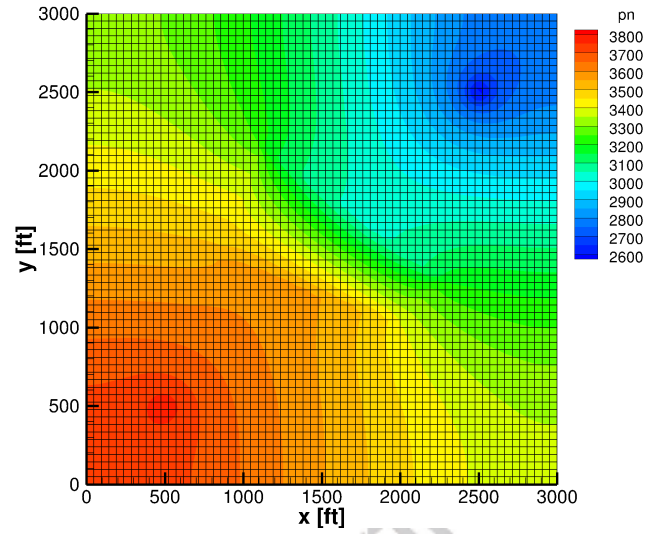


Fig. 22 Plot of p_n solution from the P1 DG method with BDF2 on a 63×63 grid with 500 timesteps ($\Delta t = 8$ days), at $t = 4000$ days.

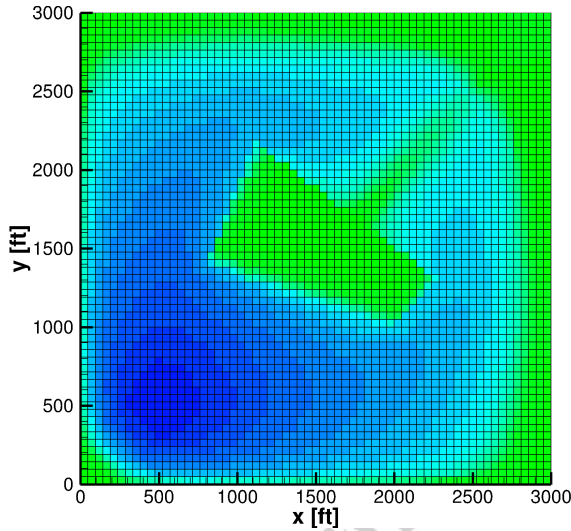


Fig. 21 Plot of S_w solution from the FV method with BDF1 on a 63×63 grid with 500 timesteps ($\Delta t = 8$ days), at $t = 4000$ days.

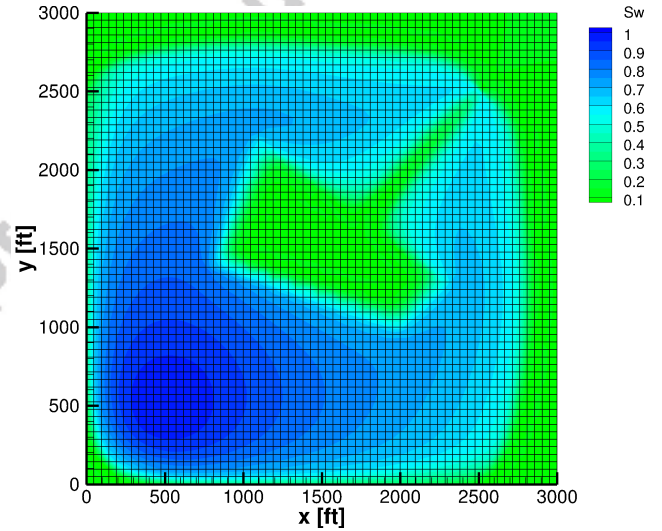


Fig. 23 Plot of S_w solution from the P1 DG method with BDF2 on a 63×63 grid with 500 timesteps ($\Delta t = 8$ days), at $t = 4000$ days.

flow equations directly for p_n and S_w . In contrast, the DG methods use the artificial viscosity formulation described in Section 5.4, and solve a coupled system of three equations. The DG methods also use the upwinding terms from Section 4. Furthermore, all three methods use the distributed well model introduced in [28, 30] for specifying the behavior of the wells, with continuity order $m = 6$, active well model radius $R = 100$ ft, and well-bore radius $r_w = 2$ inches.

Figures 20 - 21 show snapshots of the pressure and saturation solutions at the final time $t = 4000$ days, as obtained from the finite volume method on a 63×63 structured quadrilateral grid with 500 timesteps. The pressure distribution shows significant gradient changes

across the boundary of the quadrilateral block where the permeability changes discontinuously, and the saturation front is observed to flow around the low permeability region, with water breakthrough occurring at around $t = 3250$ days. The solutions from the P1 DG method with BDF2 are very similar, but slightly smoother compared to the finite volume solutions, as seen in Figures 22 - 23.

Figures 24 - 25 and 26 - 27 show contour plots of the saturation and artificial viscosity at the halfway point (i.e. $t = 2000$ days), as obtained from the P1 BDF2 and P2 BDF3 time-marching DG methods respectively. The artificial viscosity peak is observed to track the saturation front closely in both solutions, but

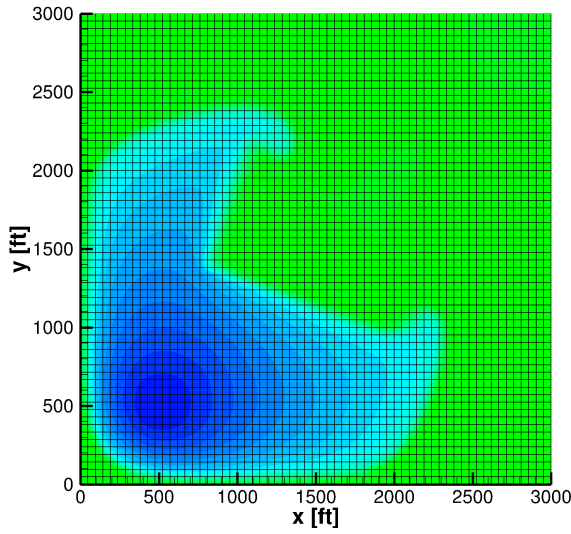


Fig. 24 Plot of S_w solution from the P1 DG method with BDF2 on a 63×63 grid with 500 timesteps ($\Delta t = 8$ days), at $t = 2000$ days.

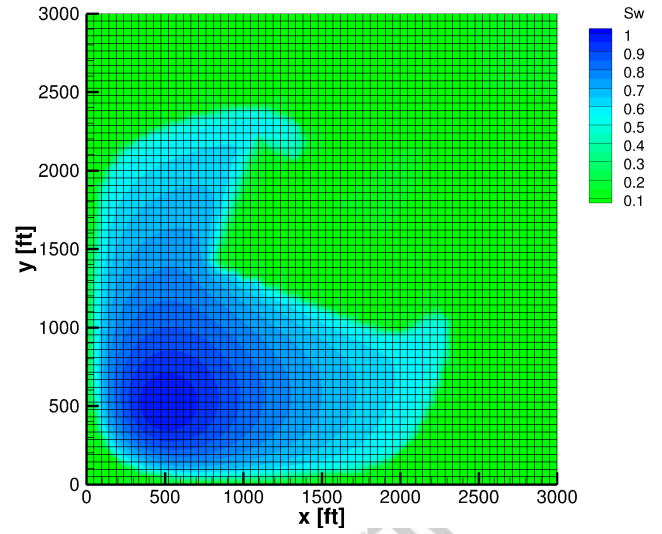


Fig. 26 Plot of S_w solution from the P2 DG method with BDF3 on a 63×63 grid with 500 timesteps ($\Delta t = 8$ days), at $t = 2000$ days.

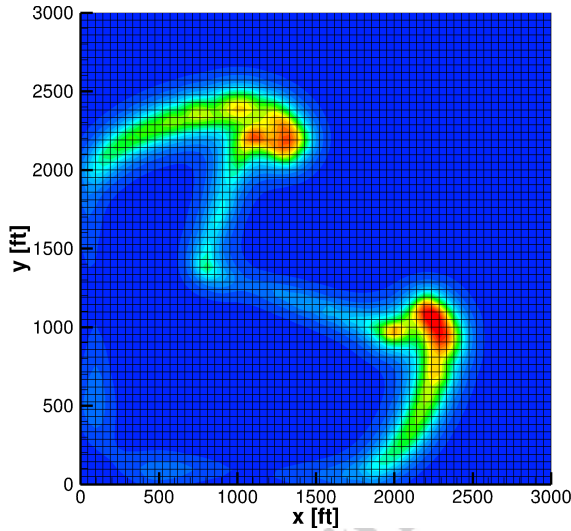


Fig. 25 Plot of ν solution from the P1 DG method with BDF2 on a 63×63 grid with 500 timesteps ($\Delta t = 8$ days), at $t = 2000$ days.

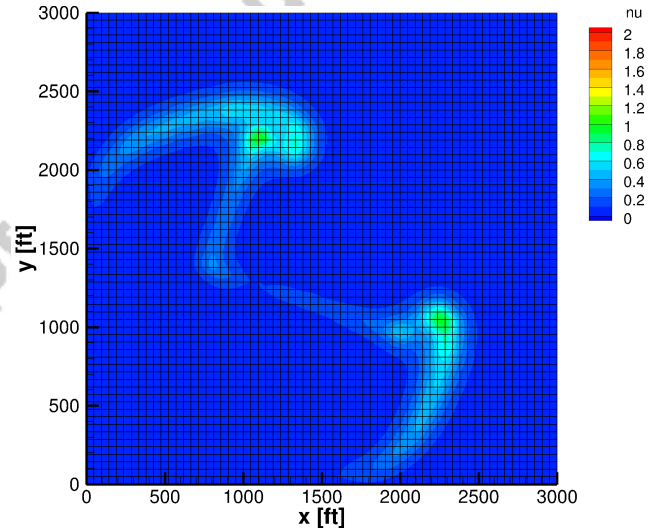


Fig. 27 Plot of ν solution from the P2 DG method with BDF3 on a 63×63 grid with 500 timesteps ($\Delta t = 8$ days), at $t = 2000$ days.

the P2 discretization requires a smaller amount of artificial viscosity on the same mesh due to its greater sub-cell resolution.

Figure 28 shows the convergence of the oil recovery factor predictions with mesh and time-step refinement. In order to make a fair comparison between the FV and DG methods, the abscissa represents the total number of space-time unknowns in each solution, given by $(N_{\text{DOF}}N_{\text{state}})$, where N_{DOF} is the number of space-time degrees-of-freedom per state variable, and N_{state} is the number of state variables used by the discretization. For the finite volume method, $N_{\text{DOF}} = N_{\text{cells}}N_t$, where N_{cells} is the number of quadrilateral cells in the mesh, and N_t is the number of time-steps used for

the simulation. Similarly for the P1 and P2 DG methods, N_{DOF} is equal to $(4N_{\text{cells}}N_t)$ and $(9N_{\text{cells}}N_t)$ respectively. Further, $N_{\text{state}} = 2$ for the finite volume method which only solves for pressure and saturation, whereas $N_{\text{state}} = 3$ for the DG methods which also solve for artificial viscosity. The time-marching finite volume method requires $\sim 10^9$ unknowns to achieve an error of $\pm 0.1\%$ in the output of interest (marked by the dotted horizontal lines). In contrast, the P1 and P2 DG methods (blue and purple lines) only require $\sim 10^8$ and $\sim 10^7$ unknowns, respectively, to achieve the same error level. This shows that higher order DG discretizations in space and time can yield significant computational savings over conventional low order methods, even af-

ter accounting for the additional degrees-of-freedom required for artificial viscosity.

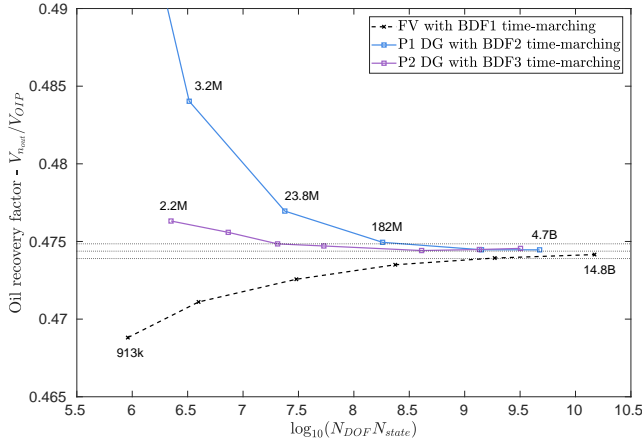


Fig. 28 Output (oil recovery factor) vs. space-time DOF for different discretizations. The upper and lower dotted horizontal lines represent an error level of $\pm 0.1\%$ relative to the true output (middle dotted horizontal line).

7 Conclusion

This paper presented work towards improving the stability and robustness of the DG discretizations, particularly for the two-phase flow equations in the advection-dominant limit. Modifications to the BR2 diffusive flux [8,9] were derived based on a linearized analysis of the analytic and discrete two-phase flow equations, which effectively upwind the underlying saturation equation. The additional interior interface terms produced from this analysis were shown to stabilize the BR2 discretization of a 1D test problem. Later, a modified form of Barter's PDE-based artificial viscosity method [5] was proposed for the Buckley-Leverett and two-phase flow equations, as a means of mitigating Gibbs oscillations that usually occur in high-order discretizations, and ensuring convergence to physical solutions. The modified DG method with artificial viscosity was demonstrated on a heterogeneous two-phase flow problem, where the high-order solutions were observed to be more computationally efficient at predicting output quantities of interest compared to conventional first-order solutions.

Although this paper only considers the BR2 diffusive flux discretization, it is expected that the upwinding terms introduced in the Section 4.3 will be equally applicable to other centered DG diffusive flux discretizations. The authors further believe that the upwinding methodology proposed here can be adapted to finite volume discretizations in the future, as an alternative to the widely used single-point upstream mobility

weighting method. The upwinding modifications and artificial viscosity formulation proposed in this paper are directly applicable to unstructured meshes [28], as well as 3D spatial problems which remain to be demonstrated in future work.

A Discrete linearized analysis

Consider the following discontinuous Galerkin weak form for the incompressible two-phase flow equations in Eqs. 1 - 2, with additional stabilization terms g_w and g_n that are yet to be determined. For simplicity, boundary conditions are ignored as the goal is the development of an upwinded interior discretization. The DG method seeks a discrete solution $\mathbf{u}_{h,p} = [p_n, S_w] \in \mathcal{V}_{h,p}$ that satisfies,

$$\begin{aligned} & \sum_{\kappa \in \mathcal{T}_h} \int_{\kappa} v \rho_w \phi \frac{\partial S_w}{\partial t} d\Omega \\ & + \sum_{\kappa \in \mathcal{T}_h} \int_{\kappa} \nabla v \cdot (\rho_w \lambda_w \mathbf{K} \nabla p_w) d\Omega \\ & - \sum_{f \in \Gamma_I} \int_f \llbracket v \rrbracket \cdot \{ \rho_w \lambda_w \mathbf{K} \nabla p_w \} d\Gamma \\ & - \sum_{f \in \Gamma_I} \int_f \llbracket v \rrbracket \cdot \{ \rho_w \lambda_w \mathbf{K} (\eta_f \vec{r}_p (\llbracket p_n \rrbracket)) \} d\Gamma \\ & - \sum_{f \in \Gamma_I} \int_f \llbracket v \rrbracket \cdot \{ \rho_w \lambda_w \mathbf{K} (-\eta_f p_{cs} \vec{r}_S (\llbracket S_w \rrbracket)) \} d\Gamma \\ & - \sum_{f \in \Gamma_I} \int_f \{ \rho_w \lambda_w \mathbf{K}^T \nabla v \} \cdot \llbracket p_n \rrbracket d\Gamma \\ & - \sum_{f \in \Gamma_I} \int_f \{ -\rho_w \lambda_w p_{cs} \mathbf{K}^T \nabla v \} \cdot \llbracket S_w \rrbracket d\Gamma \\ & + \sum_{f \in \Gamma_I} \int_f g_w(v^\pm, \mathbf{u}_{h,p}^\pm, \nabla \mathbf{u}_{h,p}^\pm; \vec{n}^+) d\Gamma = 0, \\ & \forall v \in \mathcal{V}_{h,p}, \end{aligned} \quad (69)$$

$$\begin{aligned} & \sum_{\kappa \in \mathcal{T}_h} \int_{\kappa} -v \rho_n \phi \frac{\partial S_w}{\partial t} d\Omega \\ & + \sum_{\kappa \in \mathcal{T}_h} \int_{\kappa} \nabla v \cdot (\rho_n \lambda_n \mathbf{K} \nabla p_n) d\Omega \\ & - \sum_{f \in \Gamma_I} \int_f \llbracket v \rrbracket \cdot \{ \rho_n \lambda_n \mathbf{K} (\nabla p_n + \eta_f \vec{r}_p (\llbracket p_n \rrbracket)) \} d\Gamma \\ & - \sum_{f \in \Gamma_I} \int_f \{ \rho_n \lambda_n \mathbf{K}^T \nabla v \} \cdot \llbracket p_n \rrbracket d\Gamma \\ & + \sum_{f \in \Gamma_I} \int_f g_n(v^\pm, \mathbf{u}_{h,p}^\pm, \nabla \mathbf{u}_{h,p}^\pm; \vec{n}^+) d\Gamma = 0, \\ & \forall v \in \mathcal{V}_{h,p}. \end{aligned} \quad (70)$$

All of the spatial flux terms in Eqs. 69 - 70, except for the g_w and g_n terms, are obtained by expanding the BR2 operator given in Eq. 14 for the wetting and non-wetting equations separately. The lifting operators for the primary variables p_n and S_w are represented by \vec{r}_p and \vec{r}_S respectively.

The DG weak form given by Eqs. 69 - 70 is then linearized about some base pressure distribution $\bar{p}_n(\vec{x}, t)$ and a constant

saturation value \bar{S}_w , yielding the linearized weak form of the incompressible two-phase flow equations,

$$\begin{aligned}
 & \sum_{\kappa \in \mathcal{T}_h} \int_{\kappa} v \rho_w \phi \frac{\partial S'_w}{\partial t} d\Omega \\
 & + \sum_{\kappa \in \mathcal{T}_h} \int_{\kappa} \nabla v \cdot (\rho_w \bar{\lambda}_{w_S} \mathbf{K} \nabla \bar{p}_w S'_w + \rho_w \bar{\lambda}_w \mathbf{K} \nabla p'_w) d\Omega \\
 & - \sum_{f \in \Gamma_I} \int_f \llbracket v \rrbracket \cdot \{ \rho_w \bar{\lambda}_{w_S} \mathbf{K} \nabla \bar{p}_w S'_w + \rho_w \bar{\lambda}_w \mathbf{K} \nabla p'_w \} d\Gamma \\
 & \quad - \sum_{f \in \Gamma_I} \int_f \llbracket v \rrbracket \cdot \{ \rho_w \bar{\lambda}_w \mathbf{K} (\eta_f \bar{r}'_p (\llbracket p'_n \rrbracket)) \} d\Gamma \\
 & \quad - \sum_{f \in \Gamma_I} \int_f \llbracket v \rrbracket \cdot \{ \rho_w \bar{\lambda}_w \mathbf{K} (-\eta_f \bar{p}_{c_S} \bar{r}'_S (\llbracket S'_w \rrbracket)) \} d\Gamma \\
 & \quad - \sum_{f \in \Gamma_I} \int_f \{ \rho_w \bar{\lambda}_w \mathbf{K}^T \nabla v \} \cdot \llbracket p'_n \rrbracket d\Gamma \\
 & \quad - \sum_{f \in \Gamma_I} \int_f \{ -\rho_w \bar{\lambda}_w \bar{p}_{c_S} \mathbf{K}^T \nabla v \} \cdot \llbracket S'_w \rrbracket d\Gamma \\
 & \quad + \sum_{f \in \Gamma_I} \int_f g'_w d\Gamma = 0, \\
 & \quad \forall v \in \mathcal{V}_{h,p}, \quad (71)
 \end{aligned}$$

and,

$$\begin{aligned}
 & \sum_{\kappa \in \mathcal{T}_h} \int_{\kappa} -v \rho_n \phi \frac{\partial S'_w}{\partial t} d\Omega \\
 & + \sum_{\kappa \in \mathcal{T}_h} \int_{\kappa} \nabla v \cdot (\rho_n \bar{\lambda}_{n_S} \mathbf{K} \nabla \bar{p}_n S'_w + \rho_n \bar{\lambda}_n \mathbf{K} \nabla p'_n) d\Omega \\
 & \quad - \sum_{f \in \Gamma_I} \int_f \llbracket v \rrbracket \cdot \{ \rho_n \bar{\lambda}_{n_S} \mathbf{K} \nabla \bar{p}_n S'_w \} d\Gamma \\
 & \quad - \sum_{f \in \Gamma_I} \int_f \llbracket v \rrbracket \cdot \{ \rho_n \bar{\lambda}_n \mathbf{K} (\nabla p'_n + \eta_f \bar{r}'_p (\llbracket p'_n \rrbracket)) \} d\Gamma \\
 & \quad - \sum_{f \in \Gamma_I} \int_f \{ \rho_n \bar{\lambda}_n \mathbf{K}^T \nabla v \} \cdot \llbracket p'_n \rrbracket d\Gamma \\
 & \quad + \sum_{f \in \Gamma_I} \int_f g'_n d\Gamma = 0, \\
 & \quad \forall v \in \mathcal{V}_{h,p}, \quad (72)
 \end{aligned}$$

where it is assumed that $\llbracket \bar{p}_n \rrbracket = \llbracket \bar{S}_w \rrbracket = 0$, and therefore $\bar{r}'_p(\llbracket \bar{p}_n \rrbracket) = \bar{r}'_S(\llbracket \bar{S}_w \rrbracket) = 0$.

Taking the weighted sum of the linearized weak form equations, $\rho_n \times (\text{Eq. 71}) + \rho_w \times (\text{Eq. 72})$, produces the discrete weak form of the “pressure” equation,

$$\begin{aligned}
 & \sum_{\kappa \in \mathcal{T}_h} \int_{\kappa} \nabla v \cdot \rho_w \rho_n ((\bar{\lambda}_{w_S} \mathbf{K} \nabla \bar{p}_w + \bar{\lambda}_{n_S} \mathbf{K} \nabla \bar{p}_n) S'_w) d\Omega \\
 & \quad + \sum_{\kappa \in \mathcal{T}_h} \int_{\kappa} \nabla v \cdot \rho_w \rho_n (\bar{\lambda}_w \mathbf{K} \nabla p'_w + \bar{\lambda}_n \mathbf{K} \nabla p'_n) d\Omega \\
 & - \sum_{f \in \Gamma_I} \int_f \llbracket v \rrbracket \cdot \{ \rho_w \rho_n (\bar{\lambda}_{w_S} \mathbf{K} \nabla \bar{p}_w + \bar{\lambda}_{n_S} \mathbf{K} \nabla \bar{p}_n) S'_w \} d\Gamma \\
 & \quad - \sum_{f \in \Gamma_I} \int_f \llbracket v \rrbracket \cdot \{ \rho_w \rho_n (\bar{\lambda}_w \mathbf{K} \nabla p'_w + \bar{\lambda}_n \mathbf{K} \nabla p'_n) \} d\Gamma \\
 & \quad - \sum_{f \in \Gamma_I} \int_f \llbracket v \rrbracket \cdot \{ \rho_w \rho_n (\bar{\lambda}_w + \bar{\lambda}_n) \mathbf{K} (\eta_f \bar{r}'_p) \} d\Gamma \\
 & \quad - \sum_{f \in \Gamma_I} \int_f \llbracket v \rrbracket \cdot \{ \rho_w \rho_n \bar{\lambda}_w \mathbf{K} (-\eta_f \bar{p}_{c_S} \bar{r}'_S) \} d\Gamma \\
 & \quad - \sum_{f \in \Gamma_I} \int_f \{ \rho_w \rho_n (\bar{\lambda}_w + \bar{\lambda}_n) \mathbf{K}^T \nabla v \} \cdot \llbracket p'_n \rrbracket d\Gamma \\
 & \quad - \sum_{f \in \Gamma_I} \int_f \{ -\rho_w \rho_n \bar{\lambda}_w \bar{p}_{c_S} \mathbf{K}^T \nabla v \} \cdot \llbracket S'_w \rrbracket d\Gamma \\
 & \quad + \sum_{f \in \Gamma_I} \int_f \rho_n g'_w + \rho_w g'_n d\Gamma = 0, \\
 & \quad \forall v \in \mathcal{V}_{h,p}. \quad (73)
 \end{aligned}$$

Similarly, the weighted difference of the linearized weak form equations, $\rho_n \bar{\lambda}_n \times (\text{Eq. 71}) - \rho_w \bar{\lambda}_w \times (\text{Eq. 72})$, produces the discrete weak form of the “saturation” equation,

$$\begin{aligned}
 & \sum_{\kappa \in \mathcal{T}_h} \int_{\kappa} v \rho_w \rho_n \phi (\bar{\lambda}_w + \bar{\lambda}_n) \frac{\partial S'_w}{\partial t} d\Omega \\
 & \quad + \sum_{\kappa \in \mathcal{T}_h} \int_{\kappa} \nabla v \cdot \rho_w \rho_n (\bar{\lambda}_{w_S} \bar{\lambda}_n \mathbf{K} \nabla \bar{p}_w) S'_w d\Omega \\
 & \quad + \sum_{\kappa \in \mathcal{T}_h} \int_{\kappa} \nabla v \cdot \rho_w \rho_n (-\bar{\lambda}_w \bar{\lambda}_{n_S} \mathbf{K} \nabla \bar{p}_n) S'_w d\Omega \\
 & \quad + \sum_{\kappa \in \mathcal{T}_h} \int_{\kappa} \nabla v \cdot \rho_w \rho_n (-\bar{\lambda}_w \bar{\lambda}_n \bar{p}_{c_S} \mathbf{K} \nabla S'_w) d\Omega \\
 & \quad - \sum_{f \in \Gamma_I} \int_f \llbracket v \rrbracket \cdot \{ \rho_w \rho_n (\bar{\lambda}_{w_S} \bar{\lambda}_n \mathbf{K} \nabla \bar{p}_w) S'_w \} d\Gamma \\
 & \quad - \sum_{f \in \Gamma_I} \int_f \llbracket v \rrbracket \cdot \{ \rho_w \rho_n (-\bar{\lambda}_w \bar{\lambda}_{n_S} \mathbf{K} \nabla \bar{p}_n) S'_w \} d\Gamma \\
 & \quad - \sum_{f \in \Gamma_I} \int_f \llbracket v \rrbracket \cdot \{ \rho_w \rho_n (-\bar{\lambda}_w \bar{\lambda}_n \bar{p}_{c_S} \mathbf{K} (\nabla S'_w + \eta_f \bar{r}'_S)) \} d\Gamma \\
 & \quad - \sum_{f \in \Gamma_I} \int_f \{ -\rho_w \rho_n \bar{\lambda}_w \bar{\lambda}_n \bar{p}_{c_S} \mathbf{K}^T \nabla v \} \cdot \llbracket S'_w \rrbracket d\Gamma \\
 & \quad + \sum_{f \in \Gamma_I} \int_f \rho_n \bar{\lambda}_n g'_w - \rho_w \bar{\lambda}_w g'_n d\Gamma = 0, \\
 & \quad \forall v \in \mathcal{V}_{h,p}. \quad (74)
 \end{aligned}$$

B Stability of linear ordinary differential equations

Consider the following system of linear ordinary differential equations (ODEs),

$$\mathbf{M}\dot{\mathbf{u}} + \mathbf{A}\mathbf{u} = \mathbf{b}, \quad (75)$$

where $\mathbf{u}(t) \in \mathbb{R}^m$ is the solution vector, $\mathbf{M} \in \mathbb{R}^{m \times m}$ and $\mathbf{A} \in \mathbb{R}^{m \times m}$ are constant matrices, and $\mathbf{b}(t) \in \mathbb{R}^m$ is a forcing vector. Substituting a perturbed solution $\tilde{\mathbf{u}}(t) = \mathbf{u}(t) + \mathbf{u}'(t)$ into the equation above and simplifying shows that the perturbations need to satisfy the following homogeneous equation,

$$\mathbf{M}\dot{\mathbf{u}}' + \mathbf{A}\mathbf{u}' = \mathbf{0}. \quad (76)$$

Solving this system of linear ODEs shows that the evolution of the perturbations, $\mathbf{u}'(t)$, is given by,

$$\mathbf{u}'(t) = \sum_i \hat{\mathbf{u}}'_i e^{\omega_i t}, \quad (77)$$

where ω_i and $\hat{\mathbf{u}}'_i$ are the generalized eigenvalues and eigenvectors, respectively, of the following generalized eigenvalue problem,

$$\mathbf{A}\hat{\mathbf{u}}' = -\omega\mathbf{M}\hat{\mathbf{u}}'. \quad (78)$$

It is easy to see from Eq. 77 that all generalized eigenvalues ω_i need to have negative real components for the solution perturbations to decay over time. In other words, the system of linear ODEs is stable only if $\text{Re}(\omega_i) < 0$, for $i = 1$ to m .

References

1. Aavatsmark, I.: An Introduction to Multipoint Flux Approximations for Quadrilateral Grids. *Computational Geosciences* **6**(3), 405–432 (2002)
2. Aavatsmark, I., Eigestad, G.T., Heimsund, B.o., Mallison, B., Nordbotten, J.M., Øian, E.: A New Finite-Volume Approach to Efficient Discretization on Challenging Grids. *SPE Journal* **15**(3), 658–669 (2010)
3. Arbogast, T., Juntunen, M., Pool, J., Wheeler, M.F.: A discontinuous Galerkin method for two-phase flow in a porous medium enforcing H(div) velocity and continuous capillary pressure. *Computational Geosciences* **17**(6), 1055–1078 (2013)
4. Aziz, K., Settari, A.: *Petroleum Reservoir Simulation*. Elsevier (1979)
5. Barter, G., Darmofal, D.: Shock capturing with higher-order, PDE-based artificial viscosity. *AIAA 2007-3823* (2007)
6. Bassi, F., Crivellini, A., Rebay, S., Savini, M.: Discontinuous Galerkin solution of the Reynolds averaged Navier-Stokes and $k-\omega$ turbulence model equations. *Computers & Fluids* **34**, 507–540 (2005)
7. Bassi, F., Rebay, S.: Accurate 2D Euler computations by means of a high order discontinuous finite element method, pp. 234–240. Springer Berlin Heidelberg, Berlin, Heidelberg (1995)
8. Bassi, F., Rebay, S.: GMRES discontinuous Galerkin solution of the compressible Navier-Stokes equations. In: K. Cockburn, Shu (eds.) *Discontinuous Galerkin Methods: Theory, Computation and Applications*, pp. 197–208. Springer, Berlin (2000)
9. Bassi, F., Rebay, S.: Numerical evaluation of two discontinuous Galerkin methods for the compressible Navier-Stokes equations. *International Journal for Numerical Methods in Fluids* **40**, 197–207 (2002)
10. Bastian, P.: A fully-coupled discontinuous Galerkin method for two-phase flow in porous media with discontinuous capillary pressure. *Computational Geosciences* **18**(5), 779–796 (2014)
11. Chavent, G., Cohen, G., Jaffre, J., Eyraud, R., Guerillot, D.R., Weill, L.: Discontinuous and Mixed Finite Elements for Two-Phase Incompressible Flow. *Society of Petroleum Engineers* **5**(4) (1990)
12. Cockburn, B., Hou, S., Shu, C.W.: TVB Runge-Kutta local projection discontinuous Galerkin finite element method for conservation laws IV: The multidimensional case. *Mathematics of Computation* **54**, 545–581 (1990)
13. Cockburn, B., Lin, S.Y., Shu, C.W.: TVB Runge-Kutta local projection discontinuous Galerkin finite element method for conservation laws III: One dimensional systems. *Journal of Computational Physics* **84**, 90–113 (1989)
14. Cockburn, B., Shu, C.W.: TVB Runge-Kutta local projection discontinuous Galerkin finite element method for scalar conservation laws II: General framework. *Mathematics of Computation* **52**, 411–435 (1989)
15. Cockburn, B., Shu, C.W.: The local discontinuous Galerkin method for time-dependent convection-diffusion systems. *SIAM Journal on Numerical Analysis* **35**(6), 2440–2463 (1998)
16. Cockburn, B., Shu, C.W.: The Runge-Kutta discontinuous Galerkin finite element method for conservation laws V: Multidimensional systems. *Journal of Computational Physics* **141**, 199–224 (1998)
17. Davis, T.A.: Algorithm 832: UMFPACK V4.3 - An unsymmetric-pattern multifrontal method. *ACM Transactions on mathematical software* **30**(2), 196–199 (2004)
18. Edwards, M.G., Rogers, C.F.: Finite volume discretization with imposed flux continuity for the general tensor pressure equation. *Computational Geosciences* **2**(4), 259–290 (1998)
19. Epshteyn, Y., Rivière, B.: On the solution of incompressible two-phase flow by a p-version discontinuous Galerkin method. *Communications in Numerical Methods in Engineering* **22**(7), 741–751 (2006)
20. Epshteyn, Y., Rivière, B.: Fully implicit discontinuous finite element methods for two-phase flow. *Applied Numerical Mathematics* **57**(4), 383 – 401 (2007)
21. Eymard, R., Gallouet, T., Herbin, R.: Finite volume methods. In: *Solution of Equation in \mathbb{R}^n (Part 3), Techniques of Scientific Computing (Part 3), Handbook of Numerical Analysis*, vol. 7, pp. 713 – 1018. Elsevier (2000)
22. Guermond, J.L., Pasquetti, R., Popov, B.: Entropy viscosity method for nonlinear conservation laws. *Journal of Computational Physics* **230**, 4248–4267 (2011)
23. Hartmann, R.: Numerical Analysis of Higher Order Discontinuous Galerkin Finite Element Methods. In: H. Deconinck (ed.) *VKI LS 2008-08: CFD/ADIGMA course on very high order discretization methods*. Von Karman Institute for Fluid Dynamics (2008)
24. Hartmann, R., Houston, P.: Adaptive discontinuous Galerkin finite element methods for the compressible Euler equations. *Journal of Computational Physics* **183**(2), 508–532 (2002)
25. Hoteit, H., Firoozabadi, A.: Compositional Modeling by the Combined Discontinuous Galerkin and Mixed Methods. *Society of Petroleum Engineers* **11**(1) (2006)

26. Hoteit, H., Firoozabadi, A.: Numerical modeling of two-phase flow in heterogeneous permeable media with different capillarity pressures. *Advances in Water Resources* **31**(1), 56 – 73 (2008)
27. Jayasinghe, S.: A Space-time Adaptive Method for Flows in Oil Reservoirs. Master's thesis, Massachusetts Institute of Technology, Department of Aeronautics and Astronautics (2015)
28. Jayasinghe, S.: An Adaptive Space-Time Discontinuous Galerkin Method for Reservoir Flows. PhD thesis, Massachusetts Institute of Technology, Department of Aeronautics and Astronautics (2018)
29. Jayasinghe, S., Darmofal, D.L., Burgess, N.K., Galbraith, M.C., Allmaras, S.R.: A space-time adaptive method for reservoir flows: formulation and one-dimensional application. *Computational Geosciences* **22**(1), 107–123 (2018)
30. Jayasinghe, S., Darmofal, D.L., Dow, E., Galbraith, M.C., Allmaras, S.R.: A Discretization-Independent Distributed Well Model. *SPE Journal* **24**(6), 2946–2967 (2019)
31. Jiang, J., Tchelepi, H.A.: Dissipation-based continuation method for multiphase flow in heterogeneous porous media. *Journal of Computational Physics* **375**, 307–336 (2018)
32. Jiang, J., Younis, R.M.: Efficient C1-continuous phase-potential upwind (C1-PPU) schemes for coupled multiphase flow and transport with gravity. *Advances in Water Resources* **108**, 184–204 (2017)
33. Johnson, C., Szepessy, A., Hansbo, P.: On the convergence of shock-capturing streamline diffusion finite element methods for hyperbolic conservation laws. *Mathematics of Computation* **54**(189), 107–129 (1990)
34. Klieber, W., Riviere, B.: Adaptive simulations of two-phase flow by discontinuous galerkin methods. *Computer Methods in Applied Mechanics and Engineering* **196**(1–3), 404 – 419 (2006)
35. LeVeque, R.: Numerical Methods for Conservation Laws. Lectures in Mathematics ETH Zürich, Department of Mathematics Research Institute of Mathematics. Birkhäuser Basel (1992). URL <https://books.google.com/books?id=3WhqLPcMdPsC>
36. Li, J., Riviere, B.: High order discontinuous Galerkin method for simulating miscible flooding in porous media. *Computational Geosciences* **19**(6), 1251–1268 (2015)
37. Moortgat, J., Firoozabadi, A.: Higher-order compositional modeling of three-phase flow in 3d fractured porous media based on cross-flow equilibrium. *Journal of Computational Physics* **250**, 425 – 445 (2013)
38. Moro, D., Nguyen, N., Peraire, J.: Navier-Stokes solutions using hybridizable discontinuous Galerkin methods. *AIAA* 2011-3407 (2011)
39. Nayagum, D., Schäfer, G., Mosé, R.: Modelling two-phase incompressible flow in porous media using mixed hybrid and discontinuous finite elements. *Computational Geosciences* **8**(1), 49–73 (2004)
40. Oliver, T., Darmofal, D.: Analysis of dual consistency for discontinuous Galerkin discretizations of source terms. *SIAM Journal on Numerical Analysis* **47**(5), 3507–3525 (2009)
41. Oliver, T.A.: A higher-order, adaptive, discontinuous Galerkin finite element method for the Reynolds-averaged Navier-Stokes equations. PhD thesis, Massachusetts Institute of Technology, Department of Aeronautics and Astronautics (2008)
42. Peaceman, D.: Fundamentals of Numerical Reservoir Simulation. Elsevier (1977)
43. Peraire, J., Persson, P.O.: The compact discontinuous Galerkin (CDG) method for elliptic problems. *SIAM Journal on Scientific Computing* **30**(4), 1806–1824 (2008)
44. Persson, P.O., Peraire, J.: Sub-cell shock capturing for discontinuous Galerkin methods. *AIAA* 2006-0112 (2006)
45. Rankin, R., Riviere, B.: A high order method for solving the black-oil problem in porous media. *Advances in Water Resources* **78**, 126 – 144 (2015)
46. Rivière, B.: Numerical study of a discontinuous Galerkin method for incompressible two-phase flow. In: ECCOMAS Proceedings. Finland (2004)
47. Rivière, B., Wheeler, M.F.: Discontinuous Galerkin methods for flow and transport problems in porous media. *Communications in Numerical Methods in Engineering* **18**(1), 63–68 (2002)
48. Rivière, B., Wheeler, M.F., Banaś, K.: Part II. Discontinuous Galerkin method applied to a single phase flow in porous media. *Computational Geosciences* **4**, 337–349 (2000)
49. Sesini, P.A., Coutinho, A.L.G.A.: Stabilized Finite Element Methods for Three-phase Porous Media Flows. *Mecânica Computacional* **XXIX**, 8753–8765 (2010)
50. Sesini, P.A., Souza, D.A.F.d., Coutinho, A.L.G.A.: Finite element simulation of viscous fingering in miscible displacements at high mobility-ratios. *Journal of the Brazilian Society of Mechanical Sciences and Engineering* **32**, 292 – 299 (2010)
51. Venkatakrishnan, V.: Convergence to steady state solutions of the euler equations on unstructured grids with limiters. *Journal of Computational Physics* **118**(1), 120 – 130 (1995)
52. Wang, Z., Fidkowski, K., Abgrall, R., Bassi, F., Caraeni, D., Cary, A., Deconinck, H., Hartmann, R., Hillewaert, K., Huynh, H., Kroll, N., May, G., Persson, P.O., van Leer, B., Visbal, M.: High-order CFD methods: current status and perspective. *International Journal for Numerical Methods in Fluids* **72**(8), 811–845 (2013)
53. Wheeler, M.F., Yotov, I.: A Multipoint Flux Mixed Finite Element Method. *SIAM Journal on Numerical Analysis* **44**(5), 2082–2106 (2006)
54. Wolff, M., Cao, Y., Flemisch, B., Helmig, R., Wohlmuth, B.: Multipoint flux approximation L-method in 3D: numerical convergence and application to two-phase flow through porous media, pp. 39–80. De Gruyter, Berlin, Boston (2013)
55. Yano, M.: An optimization framework for adaptive higher-order discretizations of partial differential equations on anisotropic simplex meshes. PhD thesis, Massachusetts Institute of Technology, Department of Aeronautics and Astronautics (2012)